A PHOTOELASTIC TECHNIQUE FOR THE DETERMINATION OF STRESS INTENSITY FACTORS

by

Mitchell Jolles

Dissertation submitted to the Graduate Faculty of the
Virginia Polytechnic Institute and State University in
partial fulfillment of the requirements for the degree of
DOCTOR OF PHILOSOPHY
in
Engineering Mechanics

APPROVED:

C. W. Smith, Chairman

E. G. Henneke
E. G. Henneke

M. R. Louthan

R. P. McNitt

K. L. Reifsnider
K. L. Reifsnider

July 1976

Blacksburg, Virginia

ACKNOWLEDGEMENTS

The author wishes to express his sincerest appreciation to Professor C. W. Smith for his suggestions and guidance and his unselfish extensions of advice and friendship over the past years. Gratitude is also extended to Professors E. G. Henneke, M. R. Louthan, R. P. McNitt, and K. L. Reifsnider for their contributions of time and effort.

Parts of this research were supported by the National Science Foundation under Grant No. GK-39922, the Department of Defense, U.S. Army, Contract No. DAA-F07-69-C-0444 with Watervliet Arsenal, the National Aeronautics and Space Administration under Grant No. NSG-1024 and NGR-47-004-076 from Langley Research Center, the Air Force Flight Dynamics Lab, Wright-Patterson Air Force Base under P.O. 3062 with Beta Industries, the Union Carbide Corp. Subcontract No. 7015 under W-7405-ENG-26 with the Energy Research and Development Administration.

Finally, the author wishes to thank his family and friends, and express a special indebtedness to his mother, Mrs. Sheila R. Jolles, for their unceasing interest and encouragement.

TABLE OF CONTENTS

Page

LIST OF TABLES

LIST OF FIGURES

NOMENCLATURE

x,y	Cartesian coordinates for the two dimensional problem
n,t,z	Local crack tip coordinates for the three dimensional problem
r,θ	Crack tip polar coordinates
σ_{xx}, σ_{yy}, τ_{xy}	Stress components in the x-y plane
σ_{xx}°	Stress component due to the regular stress field
σ_{nn}, σ_{zz}, τ_{nz}	Stress components in the n-z plane
σ_{nn}°, σ_{zz}°, τ_{nz}°	Stress components due to the regular stress field
α	Angle of rotation from reference to point on the flaw border
α_{max}	Maximum angle of rotation along the flaw border
ν	Poisson's ratio
ρ	Crack tip root radius
$\bar{\sigma}$	Remote loading parameter
σ_b	Bearing stress
σ_i	Stress vector
τ_{max}	Maximum in-plane shear stress
Θ_m	Coordinate of maximum radius on an isochromatic fringe
Θ_m°	Value of Θ_m at the crack tip
a	Crack depth
a_N	Crack length along reactor nozzle wall
a_V	Crack length along reactor vessel wall
A	Radius of penetrating circle for surface flaws in plates

b	Width of artificial crack
c	Flaw length
d	Distance from center of penetrating circle to plate front surface
E	Modulus of elasticity
f	Material fringe constant
g_I	Mode I strain energy release rate
J_I	Mode I path independent integral
K_I	Mode I stress intensity factor
K_{II}	Mode II stress intensity factor
K_{AP}	Mode I apparent stress intensity factor
K_{AP}^*	Combined Mode I - Mode II apparent stress intensity factor
K_{TH}	Theoretical value of the stress intensity factor
L	Plate length
n'	Isochromatic fringe order
p	Internal pressure
$\overline{r}$	Hole radius
r_m	Coordinate of maximum radius on an isochromatic fringe
r_z	Reactor vessel nominal nozzle radius
t'	Slice thickness
T	Model depth
u_i	Displacement vector
U	Strain energy density
w	Plate width

I. INTRODUCTION

Unexpected failures of high strength materials at nominal stress levels well below the yield stress of the material have plagued design engineers for many years. Investigations of such structural failures have traced the cause of failure to the presence of small cracks or crack-like flaws in the material. Thus, some knowledge of the effects of crack size and shape on structural strength must be obtained to effectively design a component. This need is enhanced by current government specifications which require that the integrity of a design not be degraded by the presence of assumed flaws in the structure.

The study of fracture mechanics originated in 1920 when Griffith [1], in his now much quoted work, published his concept of crack propagation based on an energy-rate analysis of the equilibrium of cracks. The ideas of Griffith were not utilized for metals until 1948 when Irwin [2] restated the energy concept. Nine years later Irwin [3] presented equations describing the distribution of stresses and displacements in the vicinity of a crack tip and demonstrated that the energy concept is equivalent to a "stress intensity" approach to the problem. The parameter of interest, defined by Irwin as the stress intensity factor (SIF), controls the intensity but not the distribution of the stress field surrounding a crack tip. The stress distribution in the region surrounding all crack tips is described by the same functional form for a prescribed local mode of loading. The stress intensity factor is a function of the magnitude of the loading and the geometry of the problem. Moreover, unstable crack extension occurs when the stress intensity factor reaches a critical value, which is a constant for a given material and prescribed local constraint condition; and in addition, stable crack growth due to cyclic loading has been shown [4] to be related to the stress intensity factor and material properties in many cases.

Thus, the performance of successful fracture mechanics analyses by the design engineer is dependent upon the availability of the functional relationships between the stress intensity factor and the parameters describing loading and geometry. Progress in recent years has led to the development of elasticity solutions and stress intensity factor expressions for a great number of two dimensional problems [5-7]. However, due to the complexity of the three dimensional problem, characterized by the variation of the stress intensity factor along the flaw border and crack front curvature, only limited elasticity solutions are available [8, 9]. A number of approximate, numerical and empirical techniques have been proposed for obtaining solutions to various three dimensional problems. A common approach underlying these attempts is to estimate a correction factor to a known solution of the stress intensity factor. Other formulations require the imposition of many assumptions and simplifications upon the original problem. In view of these limitations, experimental verification of stress intensity factor results obtained by the above mentioned procedures are highly desirable.

A procedure to determine values of the stress intensity factor from photoelastic data was first proposed by Irwin [10] in 1958 after observing the photoelastic fringe pattern surrounding a crack tip obtained by Post [11] and Wells and Post [12]. Several approaches for achieving results were described by Marloff and his associates [13] and the technique recommended by Irwin was utilized by Smith and his associates [14-17] and by Kobayashi and his associates [18-21]. However, extensive application of the photoelastic method has been slow to develop. This may have been due to the lack of correlation between values of the stress intensity factor obtained from photoelastic studies and accurate two dimensional analytical results.

As a consequence of these studies and others [22-25], the author [26-35] has contributed to the development of a technique for extracting values of the stress intensity factor from photoelastic data for both two and three dimensional problems. It is the purpose of this dissertation to describe the current technique and to demonstrate its accuracy and applicability to several three dimensional problems of practical interest. In particular, Chapter II describes the development of the procedure for obtaining values of the stress intensity factor from photoelastic data for the Mode I (crack opening) problem. Chapter III outlines the experimental procedure. Chapter IV assesses the accuracy of the technique and discusses the effects of using artificial cracks in the experiments and the effects of Poisson's ratio. Chapters V-VII apply the technique to obtain stress intensity factors for some three dimensional problems. Chapter VIII describes a procedure for obtaining values of the stress intensity factor from photoelastic data for the combined Mode I - Mode II (in-plane shear) problem. Chapter IX applies this technique and Chapter X contains some closing remarks.

II. ANALYTICAL FOUNDATIONS FOR THE MODE I PROBLEM

Irwin [10] described the general form of the stress field surrounding the tip of a crack subjected to in-plane loads symmetric about the plane of the crack (Mode I loading) as:

$$\begin{aligned}
\sigma_{xx} &= \frac{K_I}{(2\pi r)^{1/2}} \cos\frac{\theta}{2}\left\{1 - \sin\frac{\theta}{2}\sin\frac{3\theta}{2}\right\} - \overset{\circ}{\sigma}_{xx} \\
\sigma_{yy} &= \frac{K_I}{(2\pi r)^{1/2}} \cos\frac{\theta}{2}\left\{1 + \sin\frac{\theta}{2}\sin\frac{3\theta}{2}\right\} \\
\tau_{xy} &= \frac{K_I}{(2\pi r)^{1/2}} \cos\frac{\theta}{2}\left\{\sin\frac{\theta}{2}\cos\frac{3\theta}{2}\right\}
\end{aligned} \tag{2.1}$$

for the two dimensional problem, where the notation is described in Figure 2.1. The parameter K_I is the stress intensity factor for Mode I loading and is associated with the singular part of the elastic stress field. The second parameter, $\overset{\circ}{\sigma}_{xx}$, is related to the regular part of the elastic stress field. It is the regular part of the normal stress in the direction of crack extension at any point in the body. Since the isochromatic fringes obtained by the photoelastic method are proportional to the maximum in-plane shear stress (τ_{max}), it is desirable to compute that quantity. This is achieved through the use of equation (2.1) together with the familiar relation

$$\tau_{max} = \left\{\left(\frac{\sigma_{yy} - \sigma_{xx}}{2}\right)^2 + \tau_{xy}{}^2\right\}^{1/2} \tag{2.2}$$

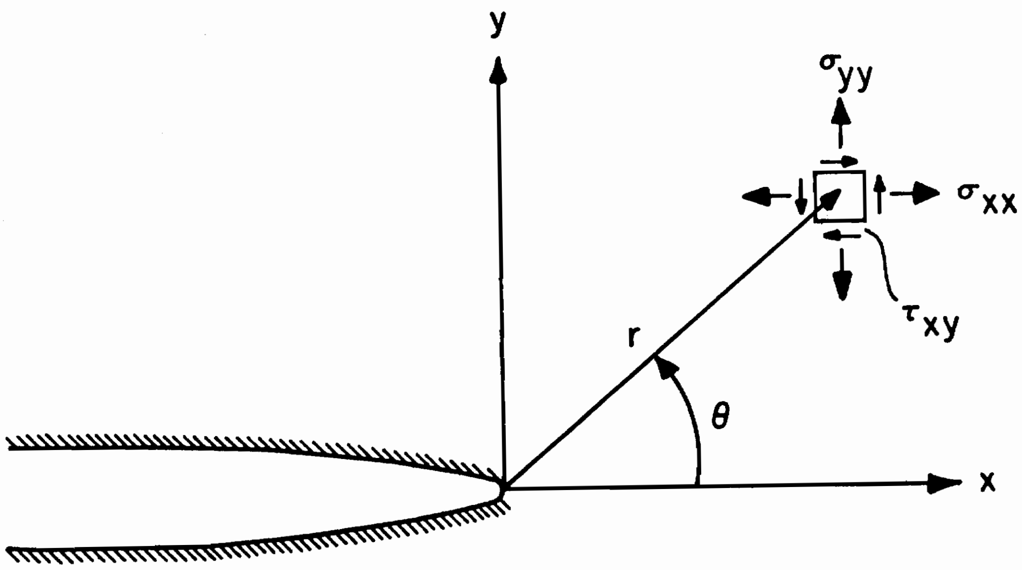

Figure 2.1 Crack Tip Stress Notation for the Two Dimensional Problem.

and results in an expression which predicts the shape of the isochromatic fringes

$$\tau_{\max} = \left\{\frac{K_I^{\,2}}{8\pi r}\sin^2\theta + \frac{K_I\overset{\circ}{\sigma}_{xx}}{(8\pi r)^{1/2}}\sin\theta\,\sin\frac{3\theta}{2} + \frac{\overset{\circ}{\sigma}{}_{xx}^{2}}{4}\right\}^{1/2} \tag{2.3}$$

Figure 2.2 shows the expected shape of a single isochromatic loop. Note that if the quantity $\overset{\circ}{\sigma}_{xx} = 0$, the fringes would tend to spread symmetrically along $\theta = \frac{\pi}{2}$. Thus, folding of the stress fringes where $\theta_m \neq \frac{\pi}{2}$ (see Figure 2.2), is caused only by the contribution of the regular part of the stress field.

Irwin's approach for obtaining values of the stress intensity factor relies upon the measurement of three quantities for a single fringe loop. For a given isochromatic, the position which is the farthest from the crack tip is located. The (r,θ) coordinate of this point is referred to as (r_m, θ_m). (See Figure 2.2.) It should be noted that the condition describing this location is

$$\frac{\partial\tau_{\max}}{\partial\theta} = 0 \tag{2.4}$$

By combining equations (2.3) and (2.4) one may obtain expressions for K_I and $\overset{\circ}{\sigma}_{xx}$ in terms of the measured quantities r_m, θ_m and $\tau_{\max}$ as

$$K_I = \frac{\tau_{\max}\sqrt{8\pi r_m}}{\sin\theta_m}\left\{1 + \frac{2\tan\frac{3\theta_m}{2}}{3\tan\theta_m}\right\}\left\{1 + \left[\frac{2}{3\tan\theta_m}\right]^2\right\}^{-1/2}$$

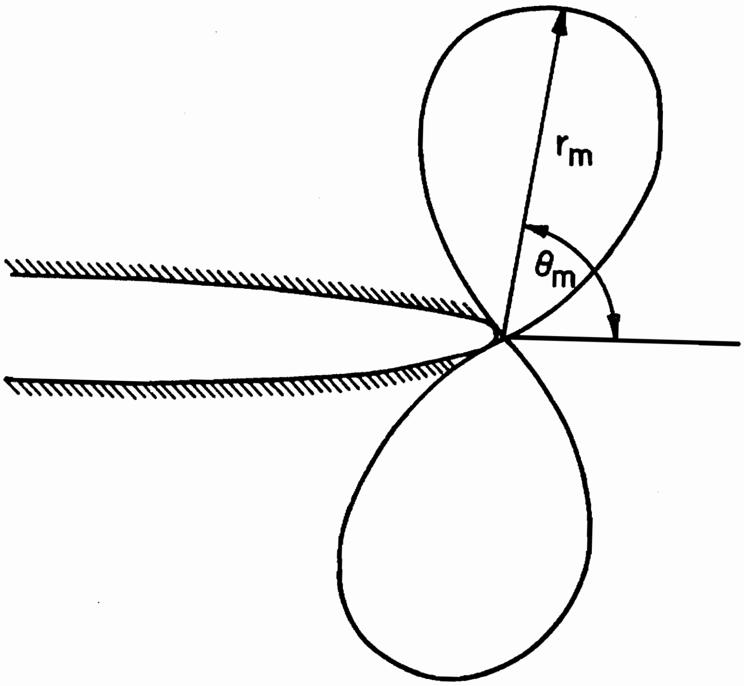

Figure 2.2 Notation for Stress Fringe Measurements.

$$\overset{\circ}{\sigma}_{xx} = \frac{2\,\tau_{max}}{\cos\frac{3\theta_m}{2}} \left\{ 1 + \left[\frac{3\tan\theta_m}{2} \right]^2 \right\}^{-1/2} \qquad (2.5)$$

The maximum in-plane shear stress is determined from the stress optic law

$$\tau_{max} = \frac{n'f}{2t'} \qquad (2.6)$$

where n' is the fringe order of the isochromatic under observation, f is the material fringe constant and t' is the thickness of the specimen.

The method, although both simple and direct, is not without drawbacks. As noted by Wells and Post in their closure to reference [10], the determination of K_I is extremely sensitive to the measurement of the angle θ_m. An error of ± 2 degrees in the measurement of a typical value of θ_m of 80 degrees results in an error of ± 9 percent in the calculation of K_I.

Marloff, et al., [13] eliminated the problem of determining $\overset{\circ}{\sigma}_{xx}$ by utilizing only values of σ_{yy} stresses along the line $\theta = 0$ to calculate K_I. Three procedures were presented for achieving the result. The values of the σ_{yy} stresses are obtained by "stress separation" of the photoelastic data. Stress separation is a tedious numerical procedure which is highly subject to inaccuracies. This could explain the scatter of ± 19% in the stress intensity factor values obtained by the three methods for a sample problem.

Subsequently, Kobayashi and his associates [18, 19] refined Irwin's technique by adopting the philosophy that since $\overset{\circ}{\sigma}_{xx}$ is due to the regular part of the stress field, the quantity may be prescribed based upon the remote loading conditions. In the absence of a full field solution, the value of σ_{xx}° would be estimated. However, Smith and his associates [14, 15] demonstrated that an error of as much as 20 percent may occur in the determination of the stress intensity factor due to an inaccurate value of the remote stress component σ_{xx}°. Their suggestion helped to alleviate the difficulties of Irwin's technique (i.e., the accurate measurement of the angle θ_m) and the approach of Kobayashi, et al. (i.e., the determination of σ_{xx}°).

The procedure suggested by Smith, et al., consisted of measuring the distance from the crack tip to two isochromatic fringes along the line $\theta = \frac{\pi}{2}$. (See Figure 2.3.) Expressions for K_I and σ_{xx}° may be obtained by solving equation (2.3) at two coordinates $(r_i, \frac{\pi}{2})$ and $(r_j, \frac{\pi}{2})$ as

$$\begin{aligned} K_I &= \sqrt{8\pi r_i}\,(\tau_{\max_i} - \tau_{\max_j})\left\{1 - (r_i/r_j)^{1/2}\right\}^{-1} \\ \sigma_{xx}^{\circ} &= \sqrt{8}\,(\tau_{\max_i} r_i^{1/2} - \tau_{\max_j} r_j^{1/2})\,(r_i^{1/2} - r_j^{1/2})^{-1} \end{aligned} \qquad (2.7)$$

As noted previously, the maximum in-plane shear stress is determined from the stress optic law, equation (2.6).

The technique for extracting values of the stress intensity factor from photoelastic data which is in current practice and is to be described and utilized in subsequent chapters of this paper is believed to be an improvement over all of the above mentioned approaches to the problem. In addition to overcoming the difficulties

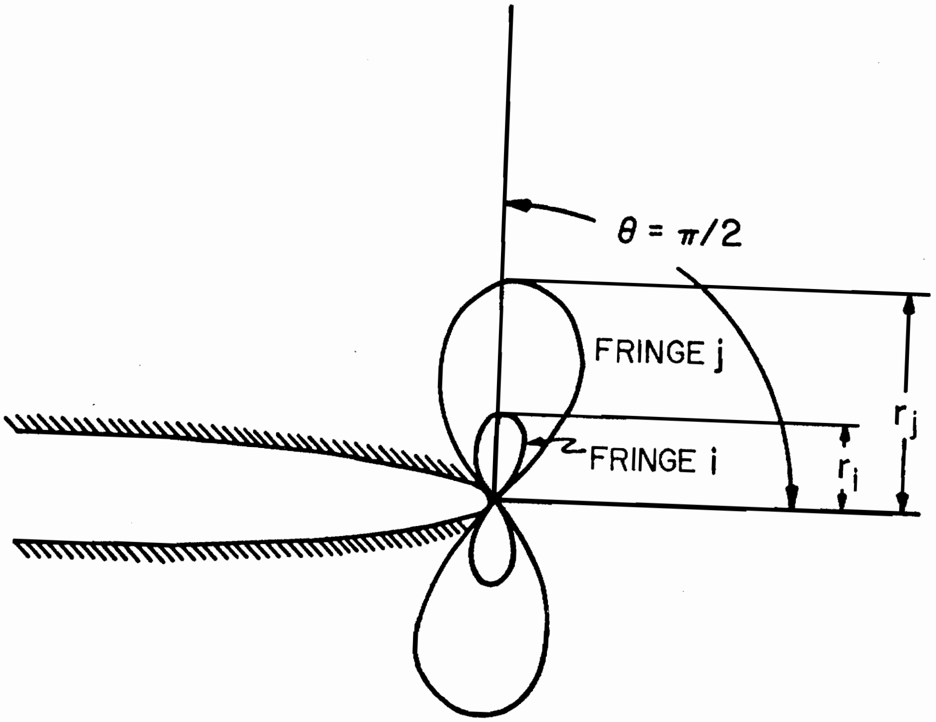

Figure 2.3 Stress Fringe Notation for the Two Fringe Technique.

and inaccuracies previously described, the technique utilizes the full field of photoelastic data together with a least squares analysis to obtain values of the stress intensity factor. Beginning as Irwin suggested, equation (2.3) may be obtained. However, observation of a typical stress fringe pattern around a crack tip under Mode I loading (see Figure 2.4) reveals that the fringes tend to spread in a direction normal to the crack line. Thus, fringe measurements may be most readily discriminated along this line. Data are taken only along $\theta = \frac{\pi}{2}$, reducing equation (2.3) to the form

$$\tau_{max} = \left\{ \frac{K_I^2}{8\pi r} + \frac{K_I \sigma_{xx}^{\circ}}{4(\pi r)^{1/2}} + \frac{\sigma_{xx}^{\circ 2}}{4} \right\}^{1/2} \tag{2.8}$$

Expanding equation (2.8) in series form and truncating the series to the same order as the original stress field equations we have

$$\tau_{max} = \frac{K_I}{(8\pi r)^{1/2}} + \frac{\sigma_{xx}^{\circ}}{(8)^{1/2}} \tag{2.9}$$

If we define an apparent stress intensity factor as

$$K_{AP} = \tau_{max}\,(8\pi r)^{1/2} \tag{2.10}$$

equation (2.9) may be rewritten as

$$K_{AP} = K_I + (\sigma_{xx}^{\circ}\pi^{1/2})r^{1/2} \tag{2.11}$$

Since it is often convenient to present values of the stress intensity factor in a normalized form, the above equation may be divided by the factor $\bar{\sigma}(\pi a)^{1/2}$ where $\bar{\sigma}$ is a parameter describing the remote loading

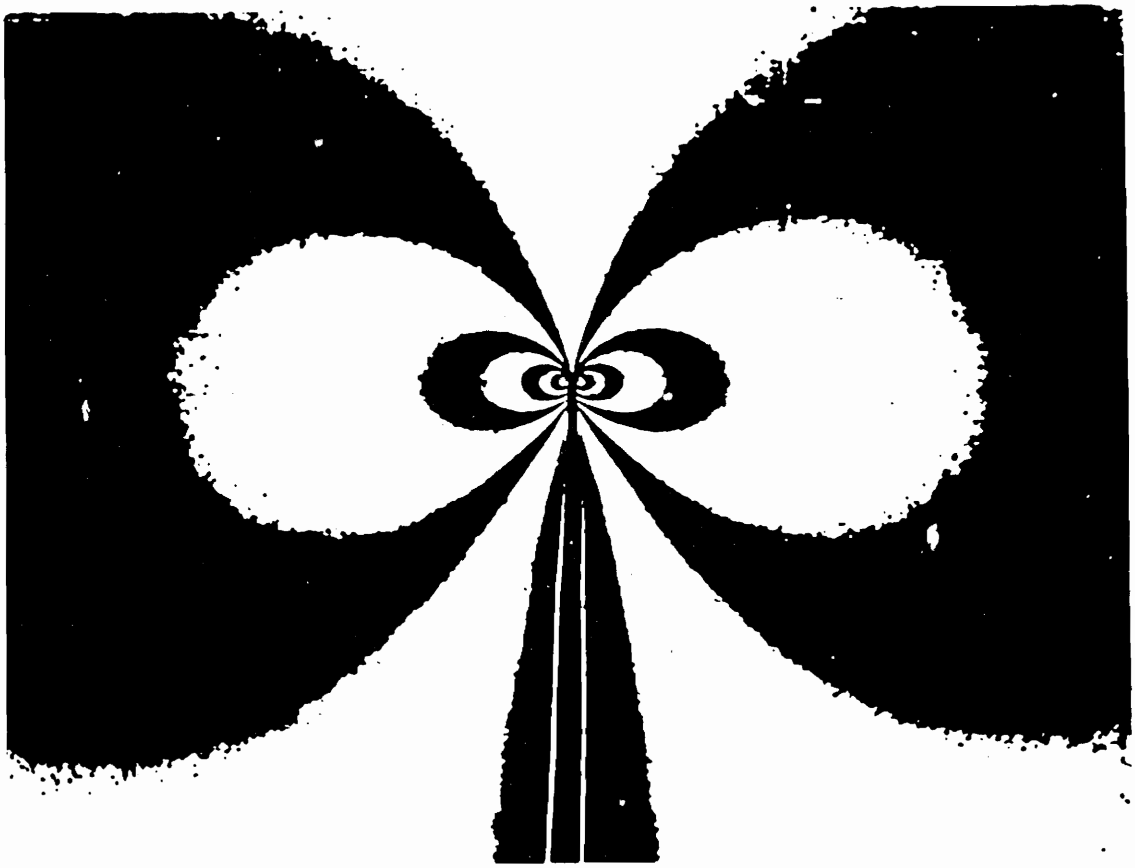

Figure 2.4 Typical Fringe Pattern for Mode I Loading.

and a is the crack length. A normalized form of equation (2.11) may then be written as

$$\frac{K_{AP}}{\bar{\sigma}(\pi a)^{1/2}} = \frac{K_I}{\bar{\sigma}(\pi a)^{1/2}} + \frac{\sigma_{xx}^{\circ}}{\bar{\sigma}} \left(\frac{r}{a}\right)^{1/2} \qquad (2.12)$$

It is important to note that if we are utilizing data taken in the region where the stress field is defined by equation (2.1), then a graph of the normalized apparent stress intensity factor versus the square root of the normalized distance from the crack tip must exhibit linear behavior. Thus, if we construct such a graph from the experimental data, and can locate a region where the data is linear, a least squares analysis will provide a straight line which can be extrapolated back to $(r/a)^{1/2} = 0$ to determine the normalized Mode I stress intensity factor. Figure 2.5 shows the result of such a plot for the Westergaard solution [36] (a through crack in an infinite plate) corrected for uniaxial tension and reveals that a linear representation is valid out to an $(r/a)^{1/2}$ of about 0.5.

The ideas utilized to derive the above technique may also be extended to establish a procedure to extract stress intensity factor values for the three dimensional problem. Kassir and Sih [37] have demonstrated that for the case of an embedded elliptical flaw, the singular stresses can be written in the same functional form as the Irwin field equations for the two dimensional problem by using a set of local coordinate axes (Figure 2.6). Sih and Liebowitz [38] have pointed out that by varying the ellipticity of such a crack, a wide variety of crack geometries of realistic shape may be achieved.

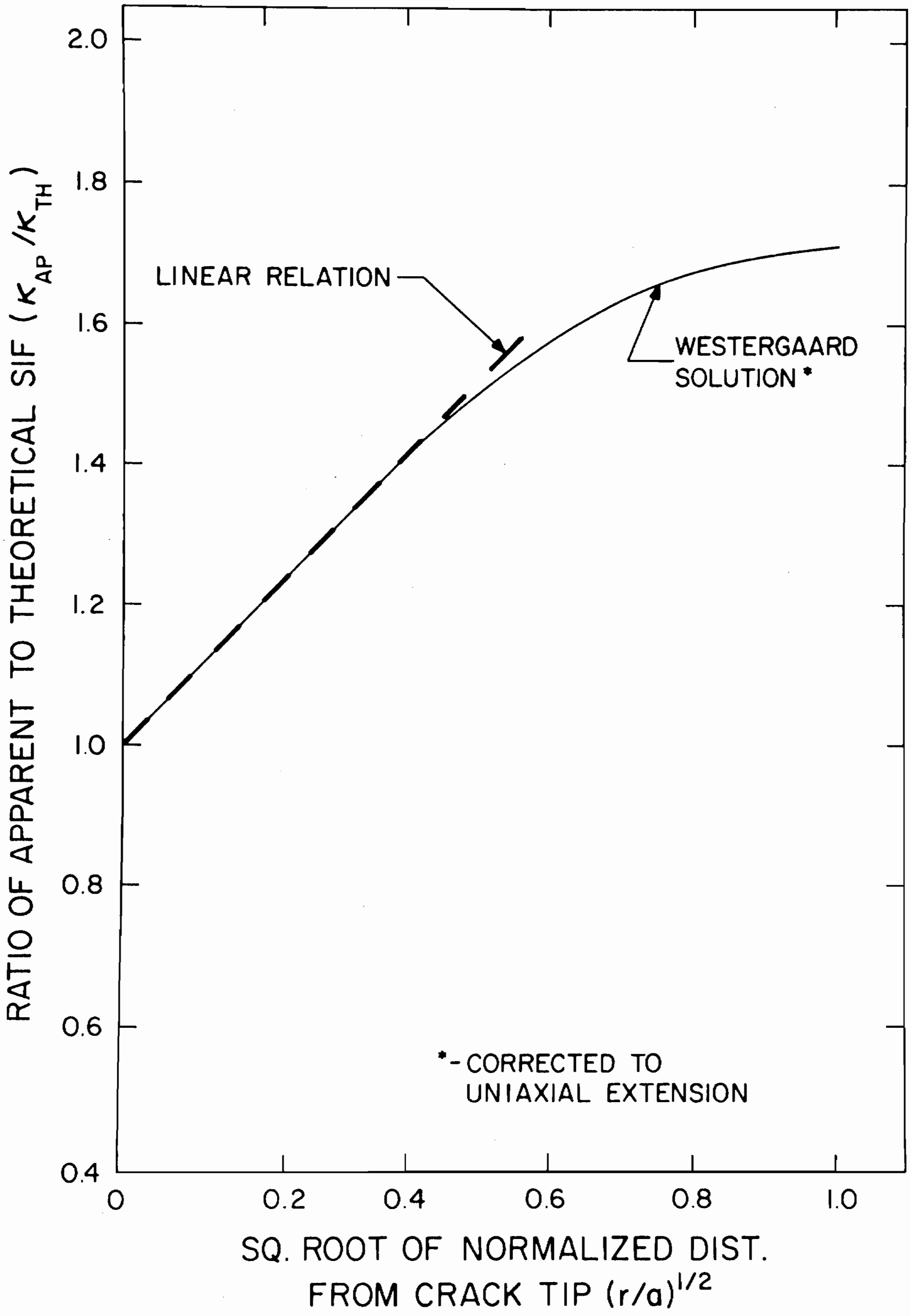

Figure 2.5 Linear Region from the Westergaard Solution.

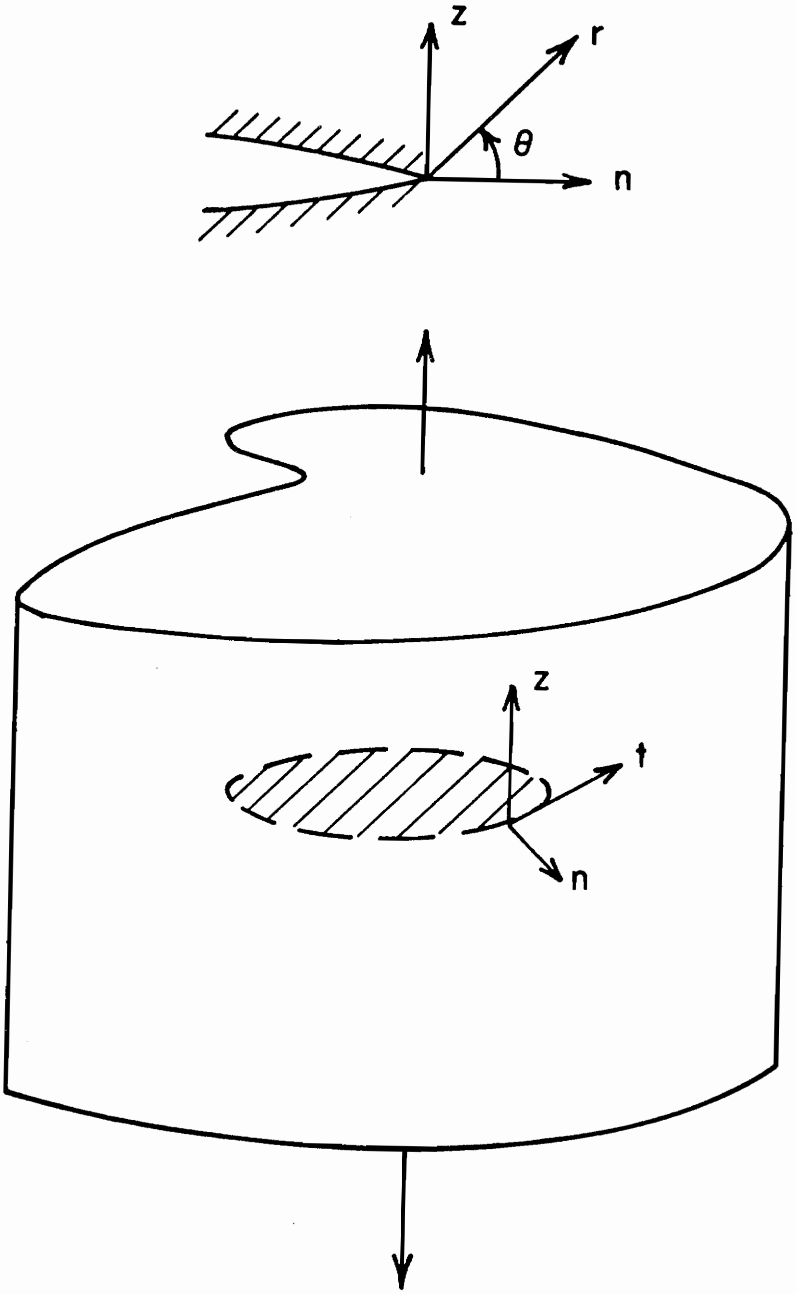

Figure 2.6 Local Crack Tip Coordinates for the Three Dimensional Problem.

Using these ideas, the local elastic stress field equations in the nz plane may be written as

$$\begin{aligned} \sigma_{nn} &= \frac{K_I}{(2\pi r)^{1/2}} \cos\frac{\theta}{2}\left\{1 - \sin\frac{\theta}{2}\sin\frac{3\theta}{2}\right\} - \sigma^{\circ}_{nn} \\ \sigma_{zz} &= \frac{K_I}{(2\pi r)^{1/2}} \cos\frac{\theta}{2}\left\{1 + \sin\frac{\theta}{2}\sin\frac{3\theta}{2}\right\} - \sigma^{\circ}_{zz} \\ \tau_{nz} &= \frac{K_I}{(2\pi r)^{1/2}} \cos\frac{\theta}{2}\left\{\sin\frac{\theta}{2}\cos\frac{3\theta}{2}\right\} - \tau^{\circ}_{nz} \end{aligned} \qquad (2.13)$$

With the notation referring to the local axes in Figure 2.6, equation (2.13) is functionally in the form of equation (2.1) but there are important differences in their interpretation. In equation (2.13), the functional expression for the stress intensity factor K_I will, in general, show that it varies along the crack border. Moreover, the values of σ°_{nn}, σ°_{zz} and σ°_{nz}, which represent the contribution of the regular part of the stress field to the components of stress near the crack tip, will also vary as one moves along the crack border, although they are treated as constants at any given point on the flaw border.

Proceeding exactly as before, we can obtain an expression for the maximum shearing stress in the nz plane from

$$\tau_{max} = \left\{\left(\frac{\sigma_{zz} - \sigma_{nn}}{2}\right)^2 + \tau_{nz}{}^2\right\}^{1/2} \qquad (2.14)$$

The above equation may be expanded in series form and truncated to the same order of the crack tip stress field equations to obtain

$$\tau_{max} = \frac{A}{r^{1/2}} + B \tag{2.15}$$

Evaluating this expression along the line $\theta = \frac{\pi}{2}$ the coefficients become

$$A = \frac{K_I}{(8\pi)^{1/2}}$$
$$B = B(\overset{o}{\sigma}_{nn}, \overset{o}{\sigma}_{zz}, \overset{o}{\tau}_{nz}) \tag{2.16}$$

The introduction of the apparent stress intensity factor defined by equation (2.10) and normalization of the subsequent equation, as in the two dimensional analysis, results in an equation similar to equation (2.12)

$$\frac{K_{AP}}{\bar{\sigma}(\pi a)^{1/2}} = \frac{K_I}{\bar{\sigma}(\pi a)^{1/2}} + \frac{B(8)^{1/2}}{\bar{\sigma}} \left(\frac{r}{a}\right)^{1/2} \tag{2.17}$$

Again, use of the photoelastic data to obtain a graph of the normalized apparent stress intensity factor versus the square root of the normalized distance from the crack tip, should reveal linear data if the data are taken in the singular stress region described by equation (2.13). By taking the full field of photoelastic data, this singular zone can be experimentally located, and, after obtaining a least squares straight line for the data in the singular zone, this line is extrapolated to $(r/a)^{1/2} = 0$. At this location, the value of the normalized apparent stress intensity factor becomes the normalized Mode I stress intensity factor as can be noted from equation (2.17).

Thus, if one wishes to obtain the stress intensity factor at some point along the border of an arbitrarily shaped plane crack, one may prepare a photoelastic model of the geometry of interest, "freeze" into the model the stress fringes under appropriate loads, and remove a slice of material containing the nz plane which can be photoelastically analyzed to determine the value of the stress intensity factor. The experimental technique is more fully described in Chapter III.

For all problems studied to date, including those presented in subsequent chapters of this paper, a linear data region (singular zone) could be located and thus the technique described above was applied to obtain stress intensity factor values. For some three dimensional problems, it is possible that non-uniform stress states, boundaries other than the crack surfaces, or crack front curvature may severely constrict the size of the singular zone, causing almost all of the experimental data to lie outside the linear data region described by equation (2.17). In order to accommodate such data, the maximum shearing stress in the nz plane may be expressed as the sum of a singular term plus a series expansion to describe the regular stress field, as

$$\tau_{max} = \frac{A}{r^{1/2}} + \sum_{n=0}^{M} B_N r^{N/2} \qquad (2.18)$$

with $A = K_I/(8\pi)^{1/2}$. Note that equation (2.18) reduces to equation (2.15) for the case $M = 0$. A suitable truncation criterion must be established for the successful application of this method.

III. EXPERIMENTAL PROCEDURE

Stress freezing photoelasticity, an experimental technique which dates back to the studies of Oppel [39], utilizes the diphase property of certain transparent materials. At room temperatures, the material exhibits viscoelastic behavior in response to loads. If one heats the material above a certain critical temperature, the material deforms elastically under load. If cooled to room temperature while under load, the load may be removed and the material may be cut into pieces without altering the stress fringes and deformations produced in the model under load at elevated temperature. By studying the photoelastic fringe patterns in appropriate slices, data can be obtained from three dimensional problems for the calculation of the stress intensity factor as outlined in the previous chapter.

There are two basic limitations in the stress freezing photoelastic method as applied to cracked bodies. The method applies only to linear elastic behavior and thus neglects nonlinearity or plasticity very near the crack tip. However, it has been found that accurate crack growth predictions can be achieved by ignoring these effects and relying on the magnitude of the elastic stress field. In addition, all stress freezing materials are incompressible ($\nu = 0.5$) above the critical temperature and thus, in this respect, do not model the basic design materials where $\nu \approx 0.3$. The effect of the elevated value of Poisson's ratio is discussed in Chapter IV.

The materials used in the experiments to be presented in this paper are Hysol 4290 (Hysol Corp.), PLM-4B (Photolastic, Inc.) and PSM-8F (Photolastic, Inc.). Although each material was, in general, satisfactory, the Hysol 4290 specimens were sometimes marred by mottling and the PLM-4B specimens required additional machining to remove a surface tension effect. PSM-8F, a recently developed material, has several advantages over the remaining two materials. PSM-8F exhibits good machinability, is free from time-edge and surface tension effects, and has a relatively low material fringe constant above the critical temperature. This is the material used exclusively in the later experiments and is the one recommended for all future work.

The stress freezing cycle generally involves the heating of the material at a moderate rate until above the critical temperature, maintaining a constant temperature for a given time period to insure uniform heating throughout the specimen, applying the load and slowly cooling to room temperature while the model is under the application of the prescribed load. Details of the thermal cycle for each material is presented in Figure 3.1. After completion of the stress freezing cycle, slices are taken mutually perpendicular to the plane of the flaw and the flaw border at desired locations. Slice thicknesses are on the order of 2 mm. The surfaces of the slice are then sanded and coated with an oil of the same index of refraction as the model material. The slice is then viewed in a circular polariscope and the necessary data are obtained.

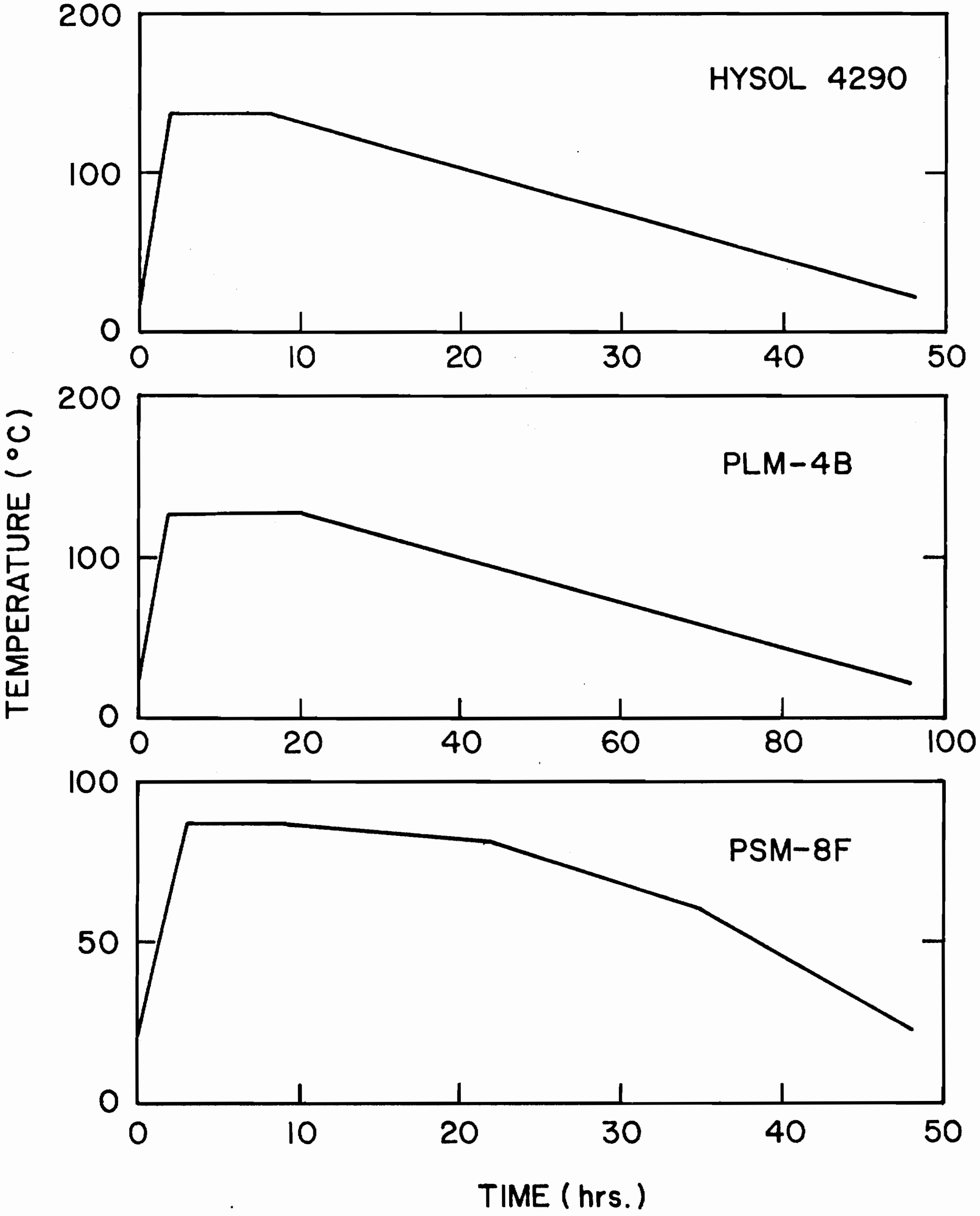

Figure 3.1 Details of the Stress Freezing Cycle.

Models were constructed from plates cut from cast sheets of the photoelastic material or by glueing sections of the model which were cast according to the specifications of the geometry. The plate tests involved loading by a string supported dead weight loading system. The cast specimens were subjected to an internal pressure as the mode of loading. The specimen geometries and particulars of the loading and experimental procedure are discussed in the latter chapters as appropriate.

Cracks are introduced into the models in either of two ways. A starter flaw is produced by tapping a thin blade against the material surface. The specimen is then heated to above the critical temperature and a load sufficient to produce crack growth is applied. The rate of crack growth is usually quite slow since the materials exhibit rubbery behavior above the critical temperature. A limitation of this method is that the shape of the flaw cannot be controlled and, in general, cannot be predicted. However, one dimension is specified to control the crack growth procedure. Flaws produced in this fashion are referred to as "natural cracks."

It is sometimes advantageous to prescribe flaw shape and dimensions; in these cases "artificial cracks" are used. Artificial cracks are obtained by machining a narrow slot into the material with a circular saw blade. A coolant should be used during the cutting operation to prevent unwanted residual machining stresses. Through the thickness cracks, flat-bottom surface flaws and part-circular surface flaws may be obtained in this manner. Two types of saw blades have been used in the experiments to be presented. The first produces a rectangular slot 152 μm in width. The second produces a 1.59 mm wide slot terminating in a triangular tip, or "V-notch", with an included angle of 30 degrees and the tip rounded to a root radius of 25 μm. The effects of using artificial cracks in the experimental work are assessed in the next chapter.

IV. CONSIDERATIONS FOR APPLYING THE METHOD

As mentioned previously, the technique described in this paper is both a clarification and an improvement over earlier methods for obtaining stress intensity factor values. However, an assessment of the technique is required in order to:

i) demonstrate the accuracy with which the stress intensity factor may be extracted from the photoelastic data;

ii) account for the influence upon local constraint of the high value of Poisson's ratio encountered in stress freezing work;

iii) determine the effects of using artificial cracks on the stress field surrounding the crack tip.

In order to accomplish this, a series of experiments were designed using an edge cracked strip as the test model. This model was selected because, due to bending effects and lack of gross constraint, it is very sensitive to small load changes and because accurate analytical solutions such as that of Gross and Srawley [40] are available. The basic specimen geometry and loading is pictured in Figure 4.1 together with the three types of cracks studied.

Stress freezing tests, with numerous replications, were conducted on each of the geometries pictured in Figure 4.1. In addition to the stress freezing tests, experiments were performed on v-notched and naturally cracked specimens at room temperature at which the material's Poisson's ratio is 0.36.

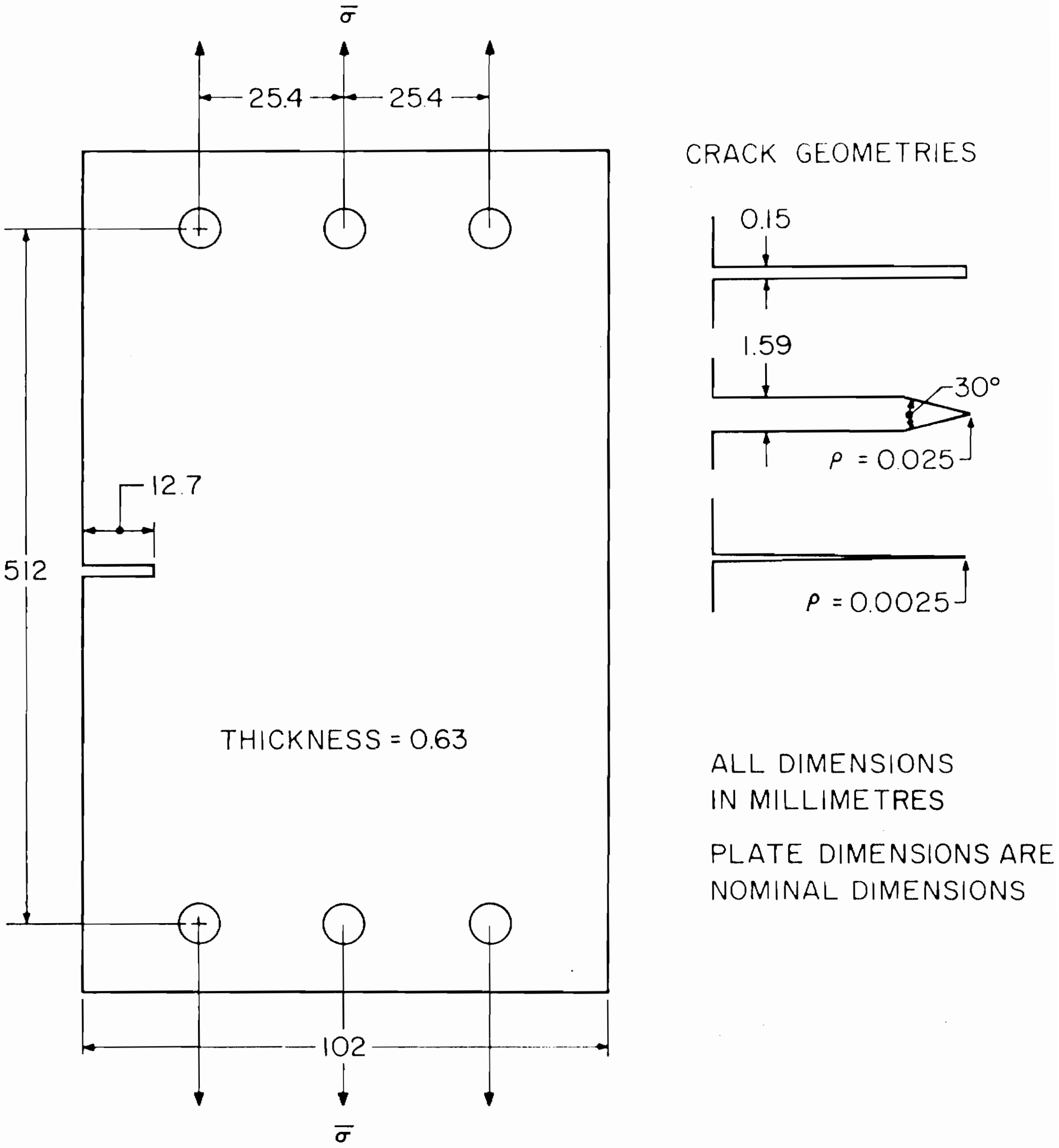

Figure 4.1 Specimen and Crack Geometries.

A set of data from one of the v-notched tests is plotted in Figure 4.2 and may be regarded as typical for all the tests. This plot of the normalized apparent stress intensity factor versus the square root of the normalized distance from the crack tip is used to interpret the data and to extrapolate the portion of the data located in the singular zone to obtain the stress intensity factor. It is apparent, from observation of Figure 4.2, that the data may be divided into three distinct regions. In Zone I, located farthest away from the crack tip, the effects of the regular stress field are significant. In Zone III, located very close to the crack tip, a stress relaxation produces a non-linear region. The exact nature of this disturbance is not clear; it may be due to finite deformations, non-linear constitutive relations, a non-linear strain-optic law for the material or a combination of these effects. Zone II is what has been called the singular zone and is the region in which the data should exhibit a linear behavior as described by equation (2.17). In general, the inner boundary of the singular zone occurs in the neighborhood of $(r/a)^{1/2} \simeq 0.2$. The outer boundary of this zone tends to extend much further out from the crack tip in problems with slowly varying effects along the flaw border. This implies a constriction of the linear zone in problems with strong three dimensional effects, and suggests a need to apply the method to several tests of a given class of problems in order to verify that the singular zone can be located experimentally for a particular problem.

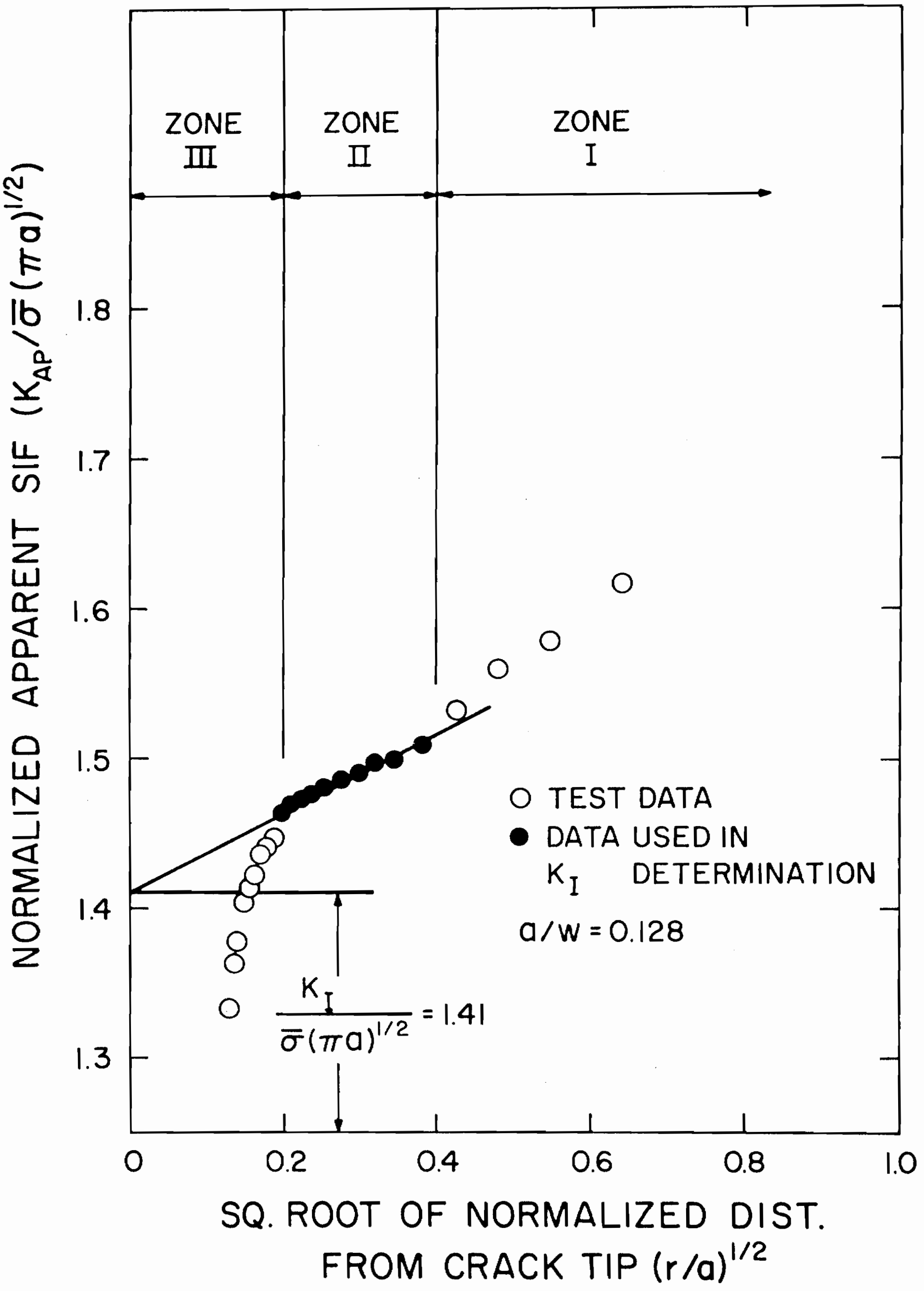

Figure 4.2 Selection of the Linear Data Zone.

A summary of the results obtained for the edge cracked plate tests is presented in Table 4.1. From a study of the average values of $\frac{K_I}{K_{TH}}$ for the stress freezing tests, it is demonstrated that the experimental results were higher than predicted by the two dimensional theory. The v-notched and naturally cracked specimens yielded essentially the same results to within the experimental reproducibility of ± 4%. The stress intensity factor values associated with the rectangular notches were greater than 20% above the analytical results. It may also be noted that the experiments conducted at room temperature produced results only slightly higher than the analytical solution. From these observations, it may be concluded that the increased values of the stress intensity factor obtained in the stress freezing tests is due to the elevated value of Poisson's ratio and that the rectangular notch alters the stress field surrounding the crack tip to produce errors in the calculation of the stress intensity factor. A further discussion of these aspects follows.

For a cracked plate of finite thickness, such as the specimen geometry under discussion in this chapter, a state of plane strain exists near the crack tip. However, remote from the crack tip the stress field and deformation field are well characterized by generalized plane stress. Since a zone of transition must lie between these extremes [41], the problem becomes three dimensional and thus dependent upon Poisson's ratio. In order to utilize two dimensional analytical solutions for comparison with stress intensity factors obtained from the inherently three dimensional experiments, Brown and Srawley [42]

TABLE 4.1

TEST RESULTS FOR EDGE CRACKED PLATES

Type of Test	Stress Freezing ($\nu = 0.5$)			Room Temperature ($\nu = 0.36$)	
Type of Flaw	Rectangular Notch	V-Notch	Natural Crack	V-Notch	Natural Crack
Number of Tests	6	7	3	2	1
Average $\frac{K_I}{K_{TH}}$	1.24	1.13	1.10	1.02	1.03
Avg. $\frac{K_I}{K_{TH}}$ (ν Corrected)	1.07	0.98	0.95	0.97	0.98

and Irwin [43] have suggested multiplying the two dimensional solution by the factor $(1 - \nu^2)^{-1/2}$. A rationale for this conversion can be constructed as follows:

Consider the Mode I traction loaded cracked plate of Figure 4.3. Rice [44] has identified an integral:

$$J = \oint_{\Gamma} \left[U dy - \sigma_i \frac{\partial u_i}{\partial x} ds \right] \qquad (4.1)$$

where $U = \int \sigma_{ij} \, d\varepsilon_{ij}$, the strain energy density, and σ_i and u_i represent, respectively, the stress and displacement vector components. Moreover, the value of the integral is independent of path for a two dimensional displacement field and is identical to the strain energy release rate g if the strain energy density is a quadratic function of the strains.

If we compute J_I for path A, which is located at distances substantially larger than the plate thickness from the crack tip, the result will be approximately the strain energy release rate related to the stress intensity factor by the plane stress result calculated by Paris and Sih [45]. Thus,

$$J_I = g_I = \frac{K_{I_A}^{\ 2}}{E} \qquad (4.2)$$

On the other hand, locating the path B within the constrained region close to the crack tip, we would expect our result to be related to the stress intensity factor by the plane strain equation

$$J_I = g_I = \frac{K_{I_B} (1 - \nu^2)}{E} \qquad (4.3)$$

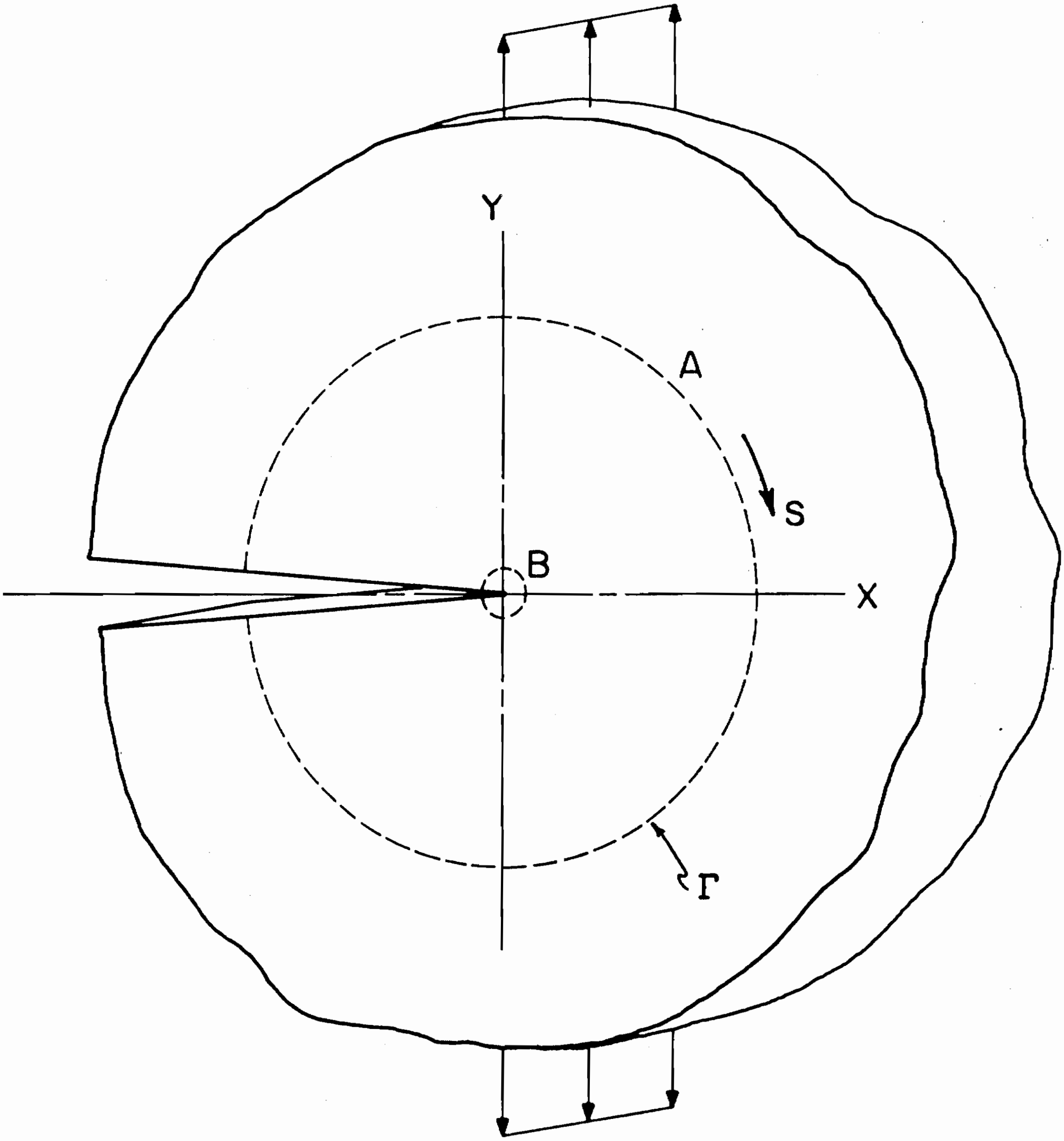

Figure 4.3 Generalized Plate Specimen.

For J_I to be path independent, it follows that

$$K_{I_B} = K_{I_A}(1 - \nu^2)^{-1/2} \tag{4.4}$$

A comparison of the experimental results with the analytical solution corrected by the application of equation (4.4) is shown in Table 4.1.

In a similar manner, the value of the stress intensity factor obtained experimentally may be corrected to account for the fact that the Poisson's ratio of the test material is different than for the prototype structural material. As an example, we may recall that in stress freezing work Poisson's ratio $\nu = 0.5$. In order to obtain the test result that would correspond to $\nu = 0.3$, the stress intensity factor value from the stress freezing experiment may first be converted to the two dimensional result by using the inverse of equation (4.4) and then converted back to a test result with $\nu = 0.3$ by applying the equation (4.4). The complete conversion factor is then $\frac{[1 - (0.5)^2]^{1/2}}{[1 - (0.3)^2]^{1/2}} = 0.91$. Thus, the stress intensity factor observed in a test specimen with a Poisson's ratio $\nu = 0.3$ is 9% lower than that observed in a stress freezing photoelastic experiment.

The effect of the elevated value of Poisson's ratio must also be accounted for when comparison is made between values of the stress intensity factor calculated from stress freezing photoelastic data for three dimensional problems and values presented in three dimensional analyses of the problems. However, since the analytical work is three dimensional, the solution is a function of Poisson's ratio and the necessary conversion factor may be derived from the analysis.

An extensive photoelastic investigation of crack-like notches was conducted by Dixon and Strannigan [46] some years ago. However, the thrust of this work was not directed toward stress intensity factor determination. The recent analytical work of Gross and Mendelson [47] shows that v-notches with an included angle of 30 degrees or less produce a crack tip stress field which leads values of the stress intensity factor to within 2% agreement with values of natural cracks. The experimental results presented here tend to confirm that statement.

The rectangular notch has been studied analytically by Schroedl and Smith [48]. Using their computer program for Savin's solution [49], Figure 4.4 was constructed. From this graph it is clear that, if the data in the range of $(r/a)^{1/2}$ between 0.2 and 0.4 is linearly extrapolated to the vertical axis, the rectangular notch ($b/a = 0.006$) produces a normalized stress intensity factor which is about 5% greater than for the line crack. After applying this result to the rectangular notch experiments presented in Table 4.1, the stress intensity factor is less than 2% above the corrected analytical value.

In addition, after accounting for the rectangular notch effects, the experimental values of the stress intensity factor average 1.3% below the corrected analytical results.

It may be concluded from this work that:

i) 1.59 mm wide slots terminating in a 30 degree triangular tip rounded to a root radius of 25 μm yield essentially the same stress intensity factor values as natural cracks.

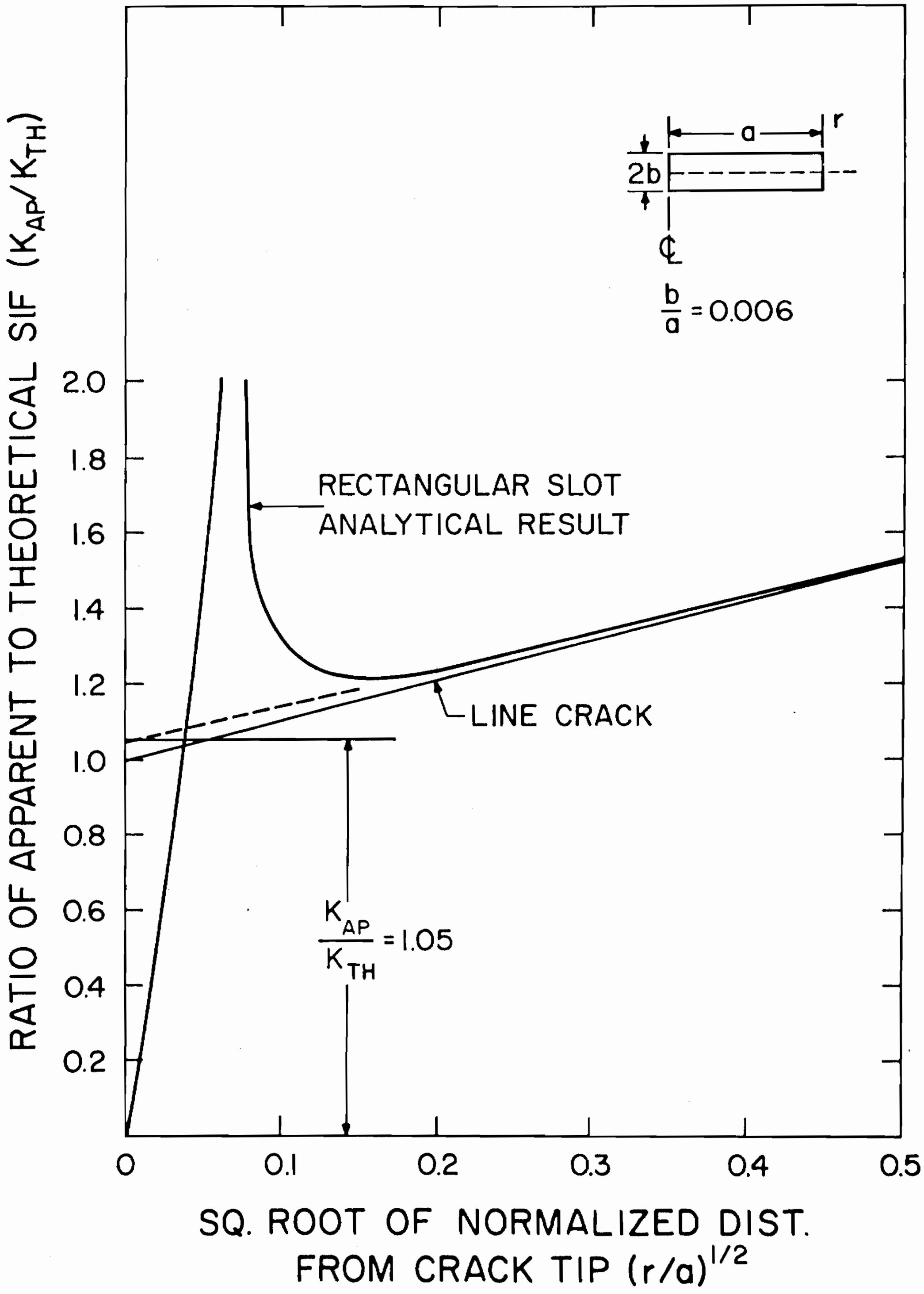

Figure 4.4 SIF Error Due to Rectangular Slot.

ii) Rectangular slots 152 μm wide tend to give stress intensity factor values which are higher than v-notch or natural crack results.

iii) The effect of Poisson's ratio in a stress freezing plate test is significant (approximately 15%) and should be accounted for when comparing results with two dimensional solutions.

iv) Test results can be replicated to within ± 4%.

v) The average experimental results compared well (to within 1.3%) with the expected stress intensity factor values.

Thus, the technique has been assessed as being a reliable experimental method for determining the value of the stress intensity factor. The application of the procedure to various three dimensional problems is presented in the following chapters.

V. APPLICATION TO SURFACE FLAWS IN PLATES

Although recognized as an important part of fatigue fracture for many years, the surface flaw was not characterized analytically until 1962, when Irwin [50], using crack opening displacements obtained by Green and Sneddon [51] for the embedded elliptical flaw, constructed an approximate expression for a semi-elliptical flaw in a half space. The stress intensity factors from this solution have been found to be accurate for shallow flaws in plates, but when the flaw penetrates to and beyond the midthickness of the plate, it becomes increasingly inaccurate due to the influence of the back surface of the plate. Inclusion of the back surface effect has been achieved through a number of approximate techniques including finite element, boundary integral, alternating, and line spring model methods, all of which are described in reference [52]. However, the problem has remained intractable to closed form solution. Moreover, while all of these methods tend towards coalescing stress intensity factor values at points of maximum flaw penetration for very shallow flaws, they yield somewhat divergent results for moderate to deep flaws in finite thickness plates.

Due to the absence of a closed form solution to the problem, one is led to consider experimental means for assessing the several approximate analytical theories. A series of stress freezing photoelastic experiments was conducted to examine the problem for a limited range of geometrical parameters. Part circular flaws (see Figure 5.1) were machined into cast plates of PSM-8F and PLM-4B. A v-notch crack tip

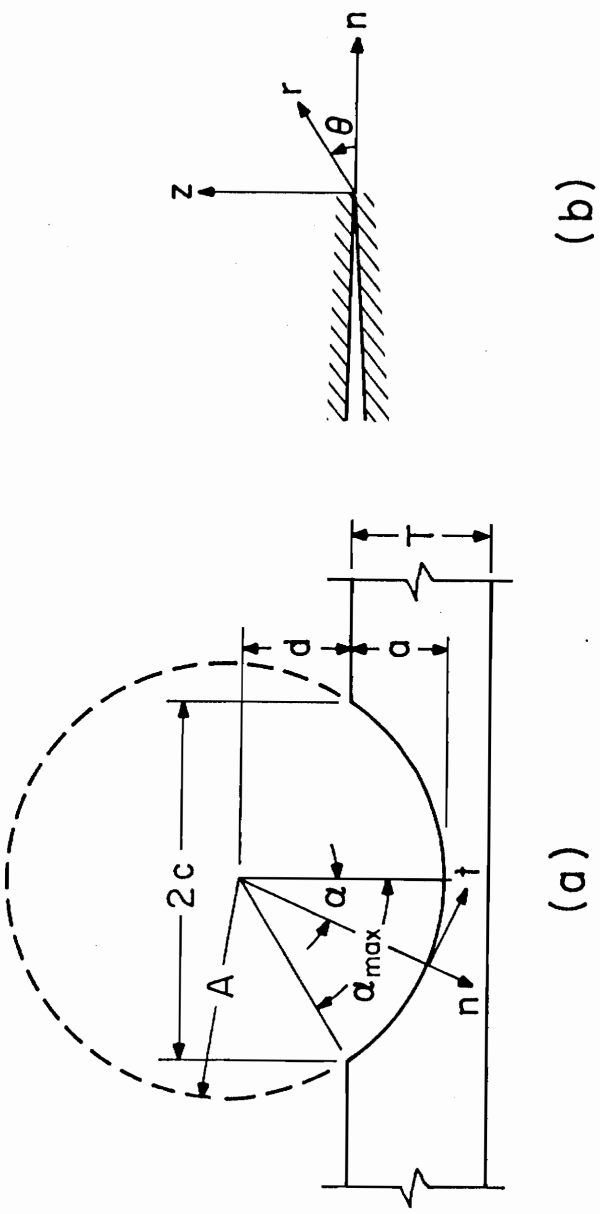

Figure 5.1 Surface Flaw Problem Geometry and Notation.

geometry, discussed in the previous chapter and diagrammed in Figure 5.2, was used. Crack lengths were kept below one fourth of the plate width to eliminate plate edge effects. Plate lengths were about three times the plate widths to insure a uniform load field above and below the flaw plane.

The test specimens were suspended in a dead weight remote tension loading rig in the stress freezing oven. After completion of the stress freezing cycle as described in Chapter 3, slices approximately 1.25 mm thick were removed from the model as indicated in Figure 5.3. Observation of the slices in a circular polariscope reveals a fringe pattern such as that shown in Figure 5.4. A typical set of data extracted from the photoelastic fringe pattern is presented in Figure 5.5 following the procedures outlined in the Appendix.

The test geometries studied and the results are given in Table 5.1. The influence of the relative crack depth a/T was studied at $d/A \simeq 0.6$. The results presented for group II represent the average of three tests. The values of the stress intensity factor were replicated to within ± 3%. Figure 5.6 presents a comparison of the experimental results with the Smith theory described in reference [53]. In computing the stress intensity factor values, the theory was adjusted to $\nu = 0.5$ by using a linear extrapolation of values presented for $\nu = 0.25$ and $\nu = 0.39$. For $\nu = 0.5$, this results in an increase in stress intensity factor values of about 6% above the values at $\nu = 0.25$. This order of increase in the stress intensity factor is also predicted by the theories of Shah and Kobayashi [54] and Rice and Levy [55].

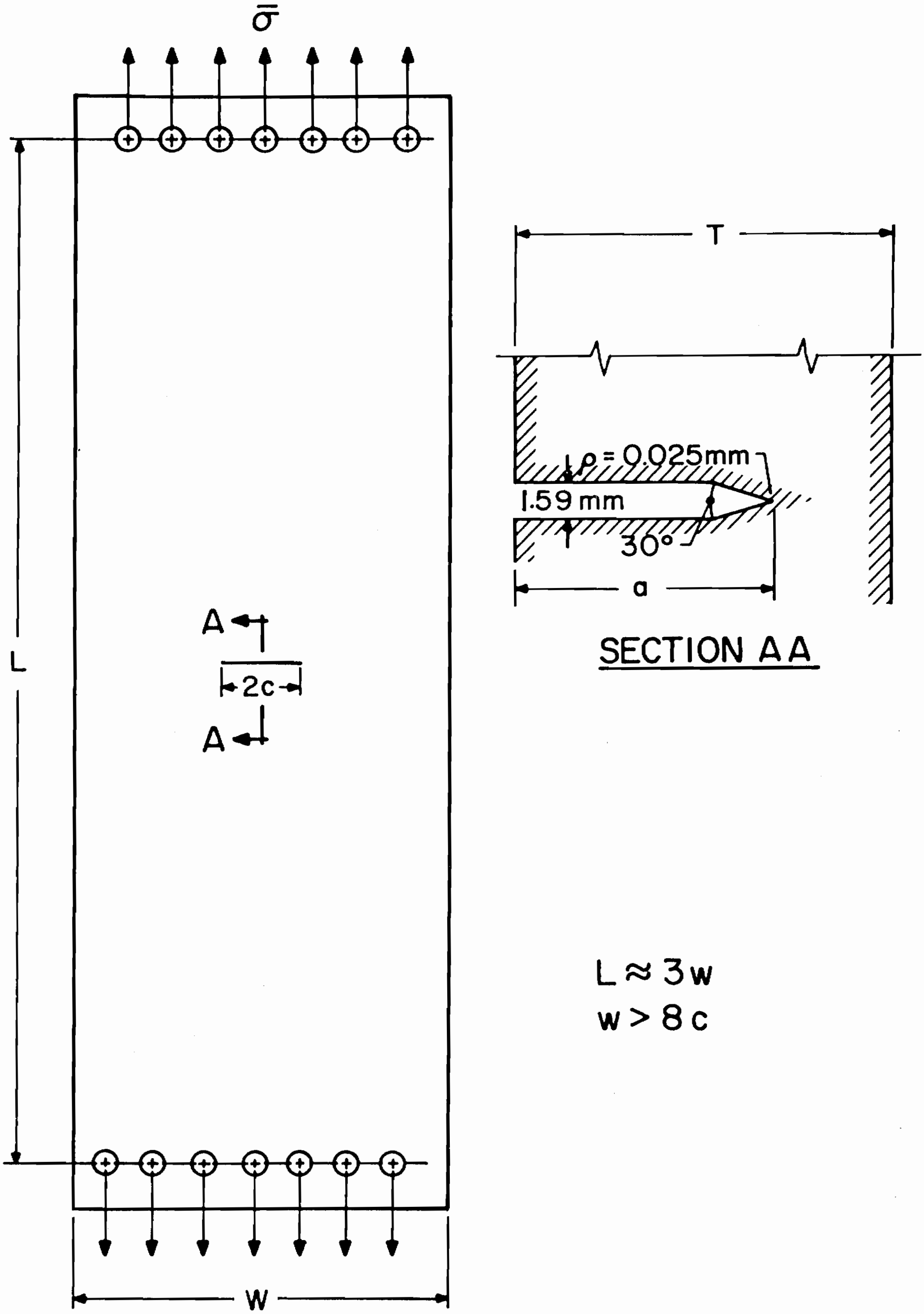

Figure 5.2 Surface Flaw Test Configuration and Crack Tip Geometry.

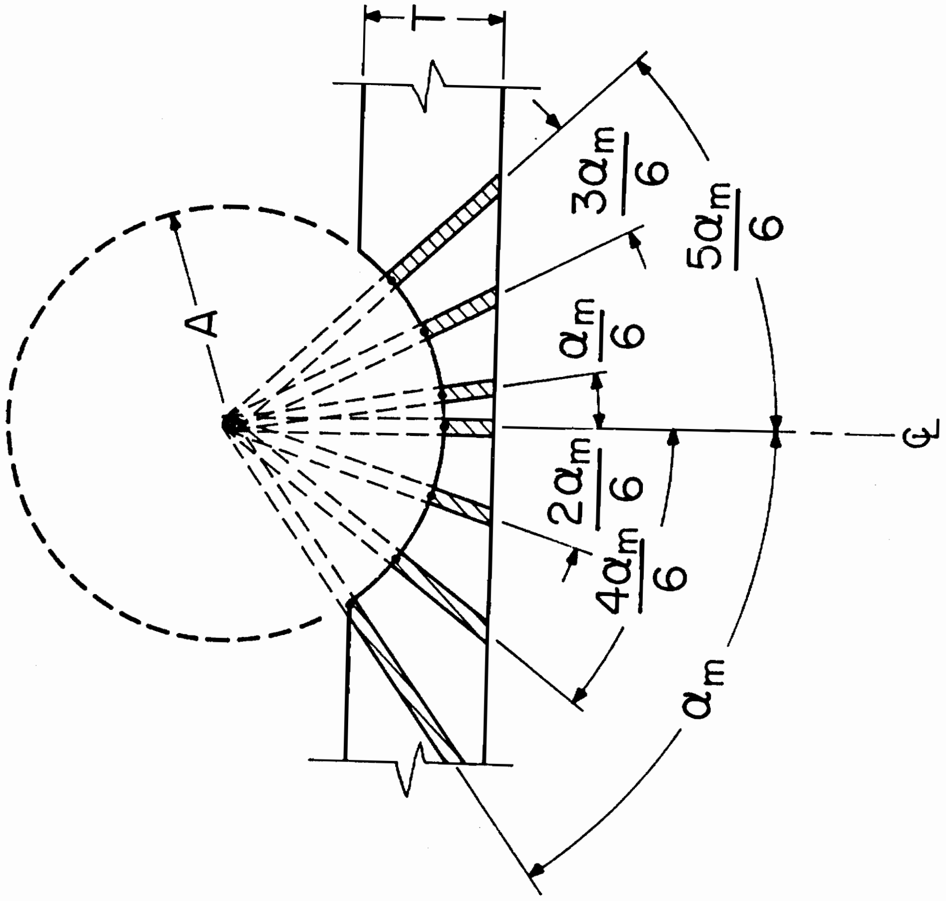

Figure 5.3 Slice Locations for the Surface Flaw Problem.

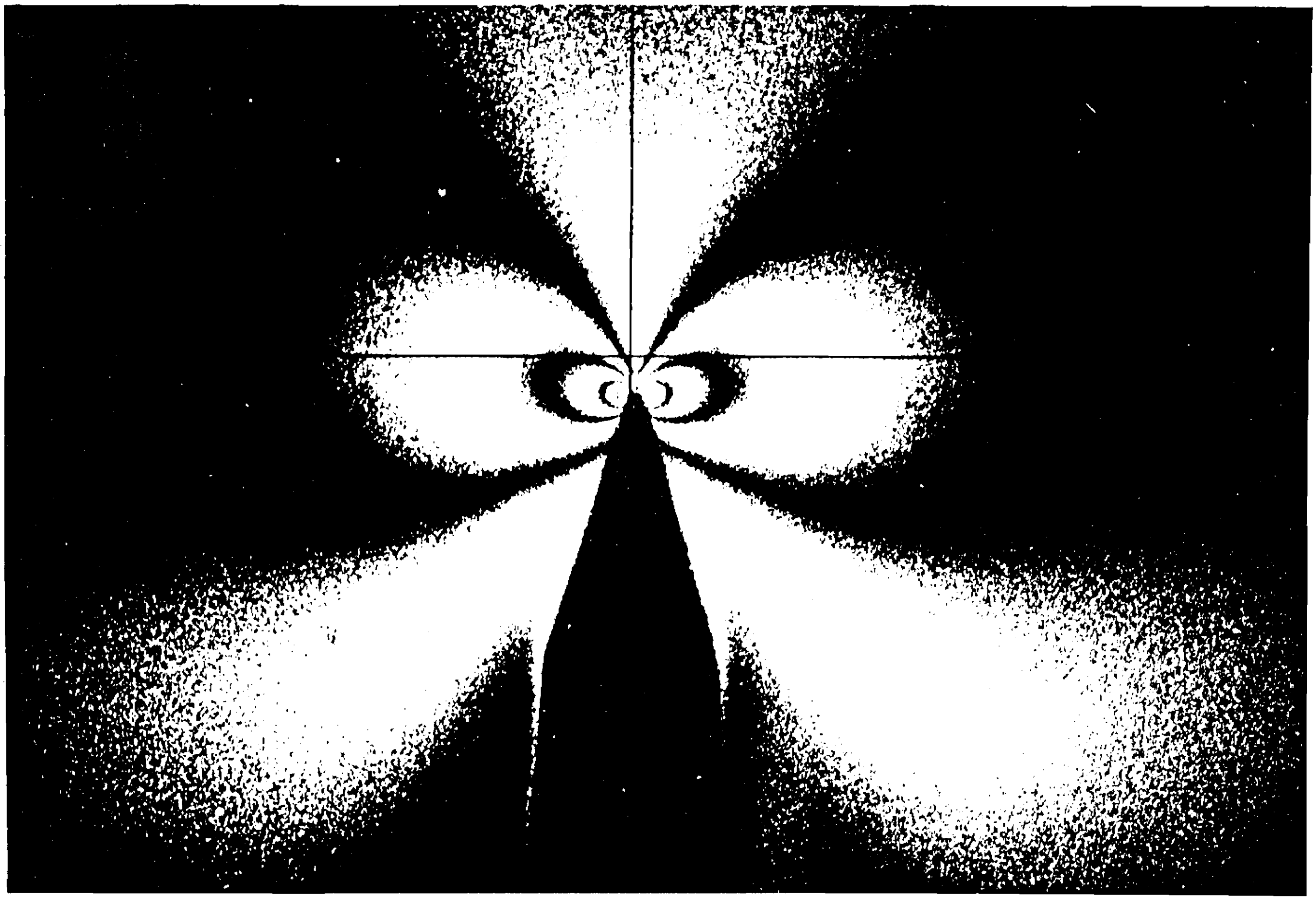

Figure 5.4 Typical Surface Flaw Fringe Pattern.

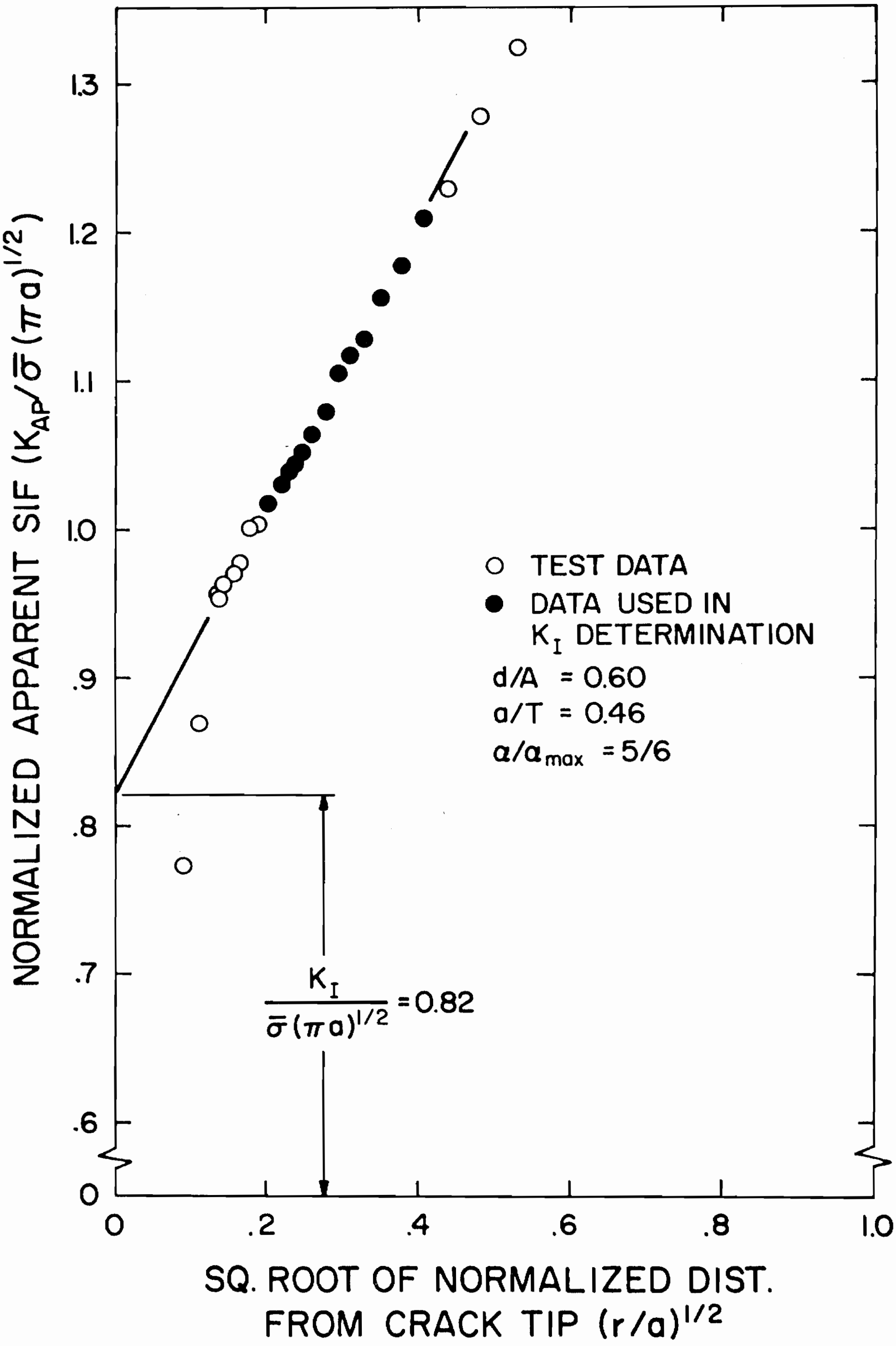

Figure 5.5 Typical Fringe Data and SIF Determination for the Plate Tests.

TABLE 5.1

TEST GEOMETRIES AND SIF VALUES FOR SURFACE FLAWS IN PLATES

GROUP	I	II^+	III
Flaw depth (a) mm	10.2	10.2	11.2
Flaw length (2c) mm	41.4	41.4	42.7
Plate thickness (T) mm	22.1	13.9	13.1
Remote stress ($\bar{\sigma}$) kPa	72.4	58.9	46.0
d/A	0.60	0.60	0.56
a/T	0.46	0.73	0.86
a/2c	0.25	0.25	0.26
$\frac{K_I}{\bar{\sigma}(\pi a)^{1/2}}$ at $\frac{\alpha}{\alpha_{max}}$ (Experiments)			
0	0.92	1.00	1.13
1/6	0.89	1.01	1.15
2/6	0.84	1.07	1.23
3/6	0.91	1.03	1.19
4/6	0.85	1.04	1.16
5/6	0.82	0.89	1.01
6/6	0.54	0.58	0.71
$\frac{K_I}{\bar{\sigma}(\pi a)^{1/2}}$ at $\frac{\alpha}{\alpha_{max}} = 0$ $(\nu = 0.5)$			
Experimental	0.92	1.00	1.13
Shah-Kobayashi	0.89	1.00	1.10
Rice-Levy	1.12	*	*
Newman	1.00	1.17	1.30
Smith-Sorensen	0.96	1.07	1.17

All tests: Radius of penetrating circle, A, mm 25.4
Plate width, w, mm 177.

+ This group represents the average of three tests.

* These geometries are outside the range of this theory.

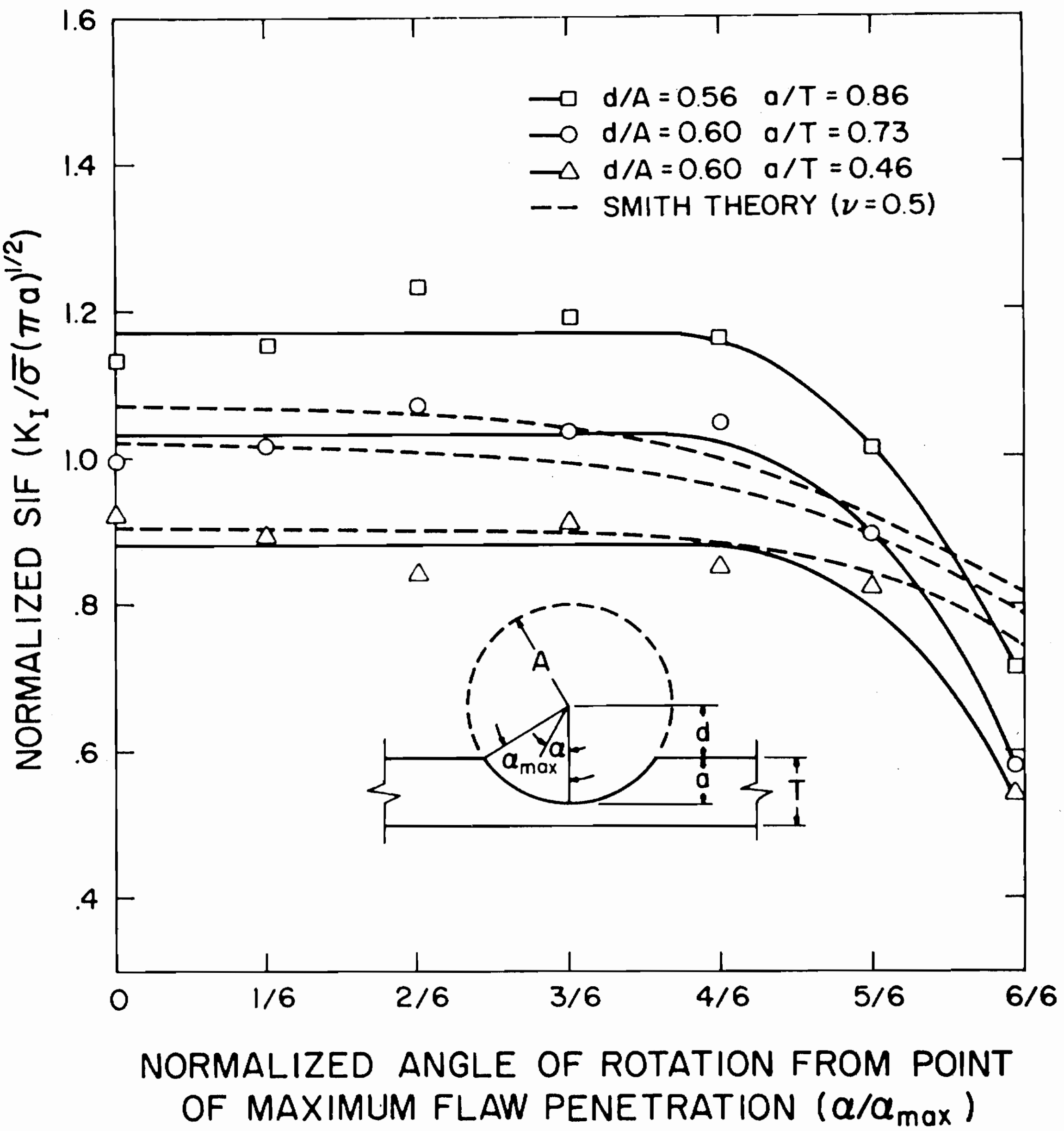

Figure 5.6 SIF Distribution Along the Plate Flaw Border.

Figure 5.6 shows that the Smith analysis overestimates the stress intensity factor values significantly at points near where the flaws intersect the front surface of the plates. However, near points of maximum flaw penetration, agreement with experimental results to within 5% was observed for a/T = 0.46 and 0.73. For a/T = 0.86, the theory underestimates the stress intensity factor at points of maximum flaw penetration by about 10%.

In addition to the above comparisons with Smith's work, the experimental values of the stress intensity factor at the point of maximum flaw penetration were compared with several semi-elliptical surface flaw theories [54-57] by matching flaw depth and length. The results are shown in the lower part of Table 5.1. The best agreement for the geometries studied here is found with the Shah and Kobayashi analysis where the results compared to within 4%.

VI. APPLICATION TO FLAWED REACTOR VESSEL-NOZZLE INTERSECTIONS

The incidence of cracks at the juncture of pipes with reactor vessel housings has been a persistent problem in the pressure vessel and piping industry for many years. Experience has shown, however, that such cracks can be tolerated without rendering the structure inoperative provided adequate estimates of the stress fields surrounding the crack tip, characterized by the stress intensity factor, can be made. Stress freezing photoelastic models of nuclear reactor pressure vessels were constructed containing a crack at the intersection of the nozzle wall and vessel wall to conduct an experimental program to obtain such information. The test procedure involved:

i) Using PSM-8F as the specimen material, cast sections of the model to the required geometric specifications.

ii) Introduce a natural crack into the inside corner of the juncture of the nozzle wall with the vessel wall.

iii) Assemble the entire model as pictured in Figure 6.1.

iv) Heat to above the critical temperature, apply an internal pressure and grow the crack to the desired size, reduce the pressure to a level to insure no further crack growth and cool to room temperature.

v) Obtain slices mutually orthogonal to the flaw surface and flaw border at appropriate locations.

The notation adopted for the current problem is presented in Figure 6.2. The four tests conducted cover a range of a/T of 0.15 to 0.71. The crack dimensions are outlined in Table 6.1. It should be

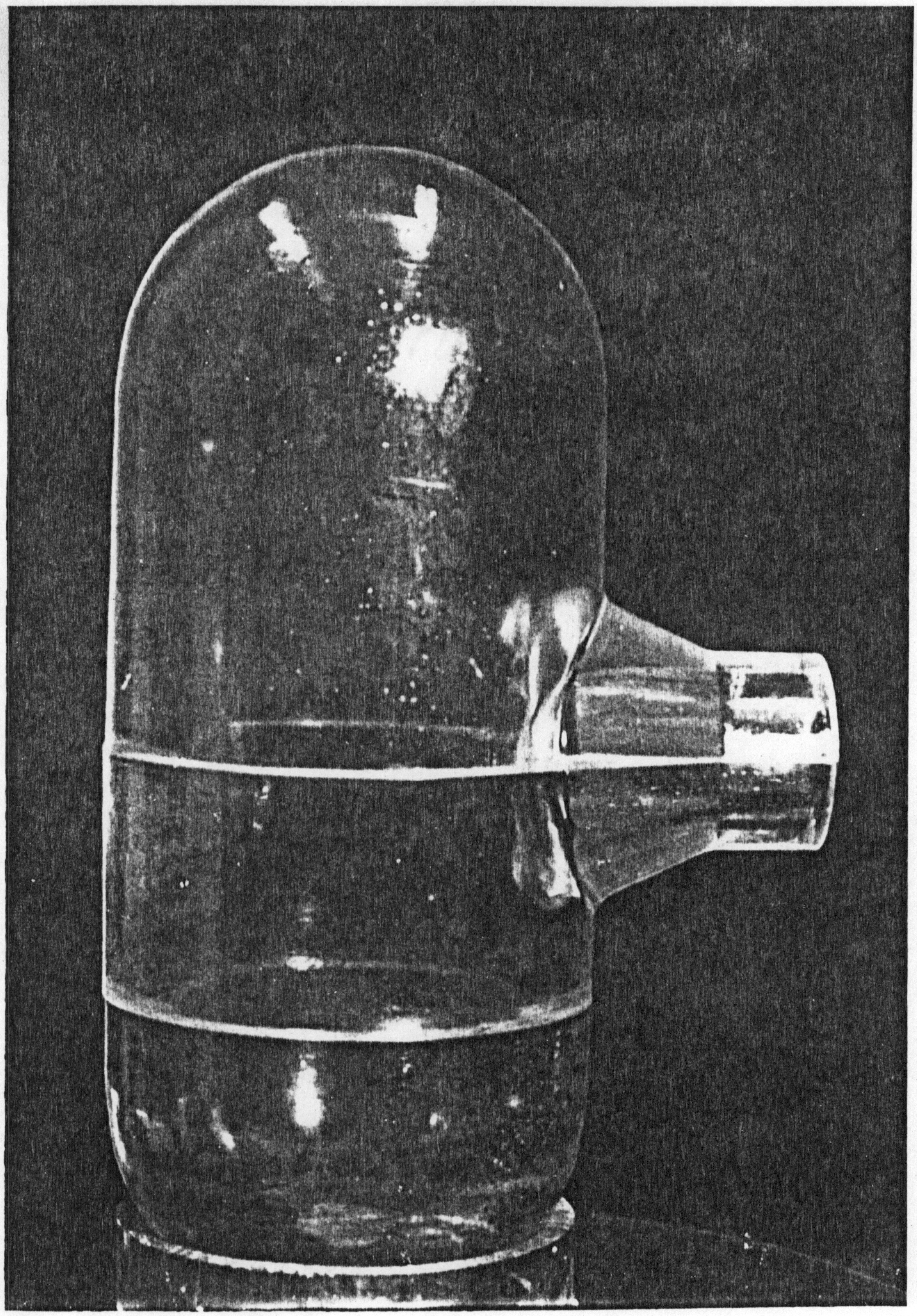

Figure 6.1 Reactor Vessel Model.

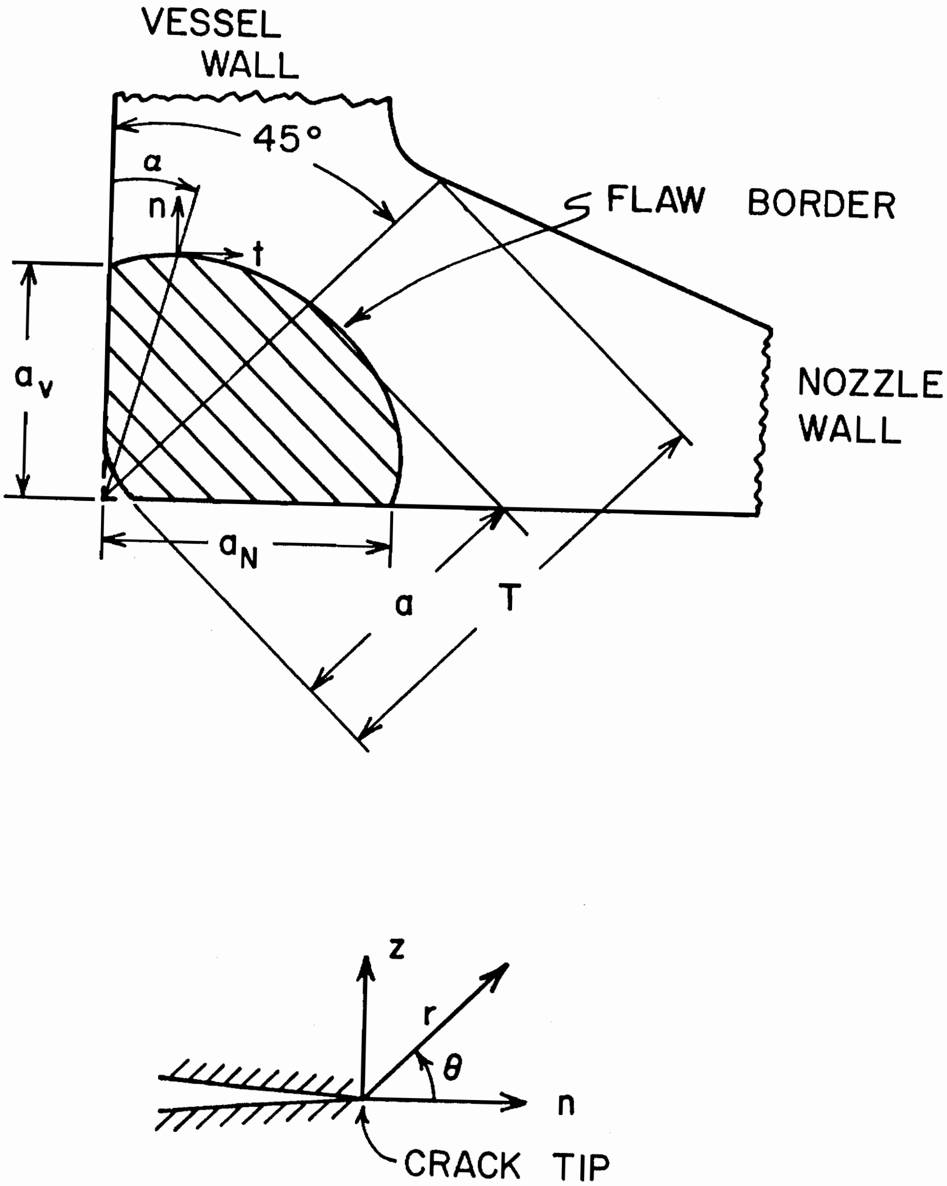

Figure 6.2 Reactor Vessel Problem Geometry and Notation.

TABLE 6.1

FLAW GEOMETRIES FOR THE REACTOR VESSEL TESTS

Test Number	1	2	3	4
Vessel wall crack length (a_V) mm	5.6	14.0	18.3	36.3
Nozzle wall crack length (a_N) mm	5.6	14.0	18.5	26.6
Crack depth (a) mm	4.8	11.9	15.5	22.4
a/T	0.15	0.37	0.48	0.71

All tests: T = 31.8 mm.

noted that although the flaw borders remain normal to the vessel and nozzle walls, their shape changes from quarter-circular for the shallow flaws to a shape with very little curvature of the flaw border in the central region of the flaw border as the crack depth increases.

Viewing a slice in a circular polariscope, one would observe a fringe pattern such as that pictured in Figure 6.3. Utilization of the photoelastic data for the determination of the stress intensity factor is demonstrated in Figure 6.4.

It is difficult to quantitatively compare the results of the experiments with current finite element solutions due to differences in nozzle geometries. However, qualitative comparisons of stress intensity factor distributions along the flaw border would seem to be appropriate. Figure 6.5 shows the normalized stress intensity factor distributions along the flaw borders. Upon comparing these trends with those presented in references [58] and [59], the finite element solutions predict an increase in the stress intensity factor near the points of intersection of the flaw border with the vessel or nozzle wall while the experiments clearly show a decrease in the stress intensity factor at these locations.

Quantitative comparisons may be made between the present results and previous experimental work conducted by Derby [60], since the two reactor vessel models are virtually the same geometry. Derby also used plastic models, in which he extended his cracks from initial slots by fatiguing. This process was followed by residual static strength tests. Since Derby was able to report only one value of the stress

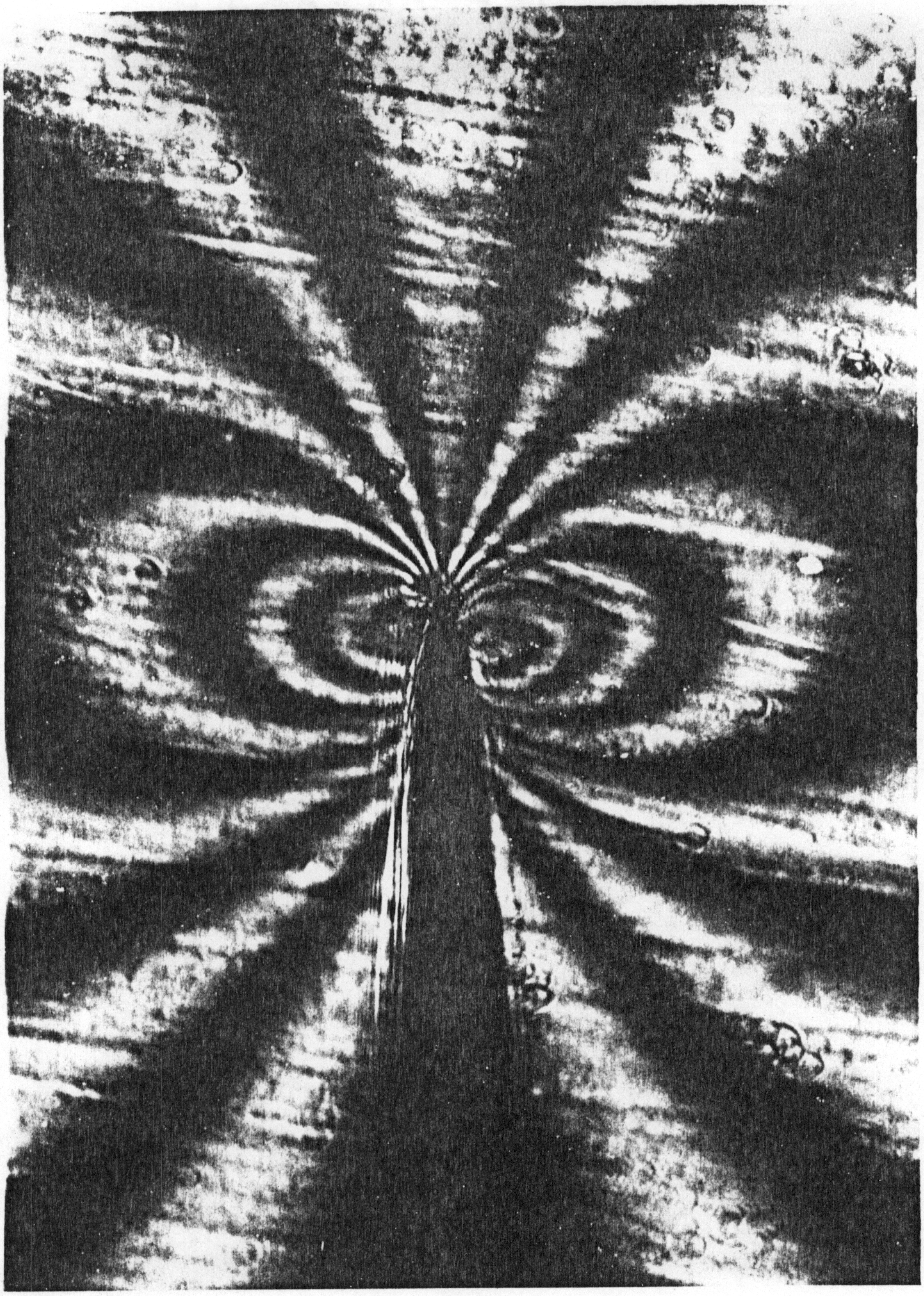

Figure 6.3 Typical Fringe Pattern for Reactor Vessel Crack.

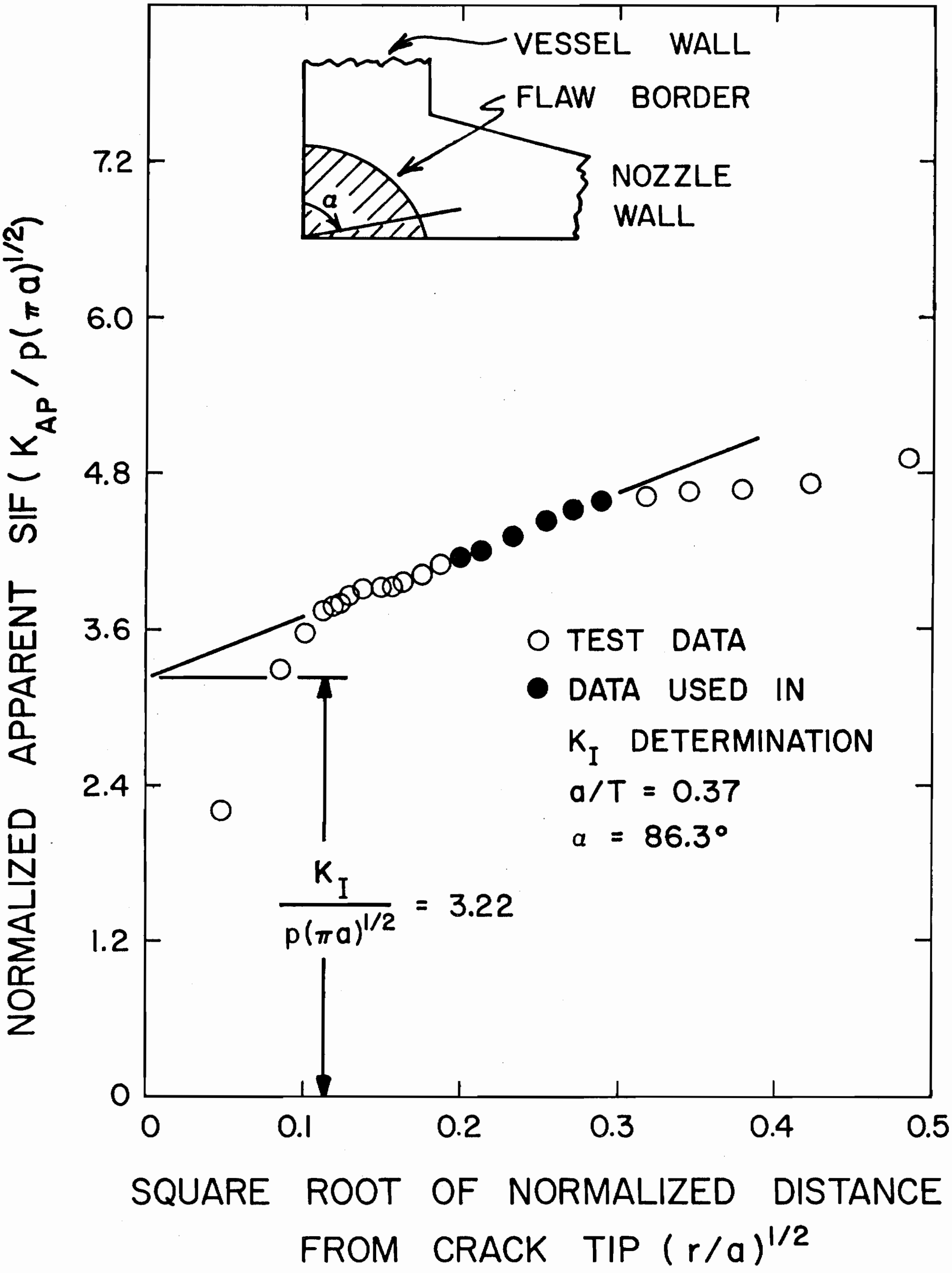

Figure 6.4 Typical Reactor Vessel Fringe Data and SIF Determination.

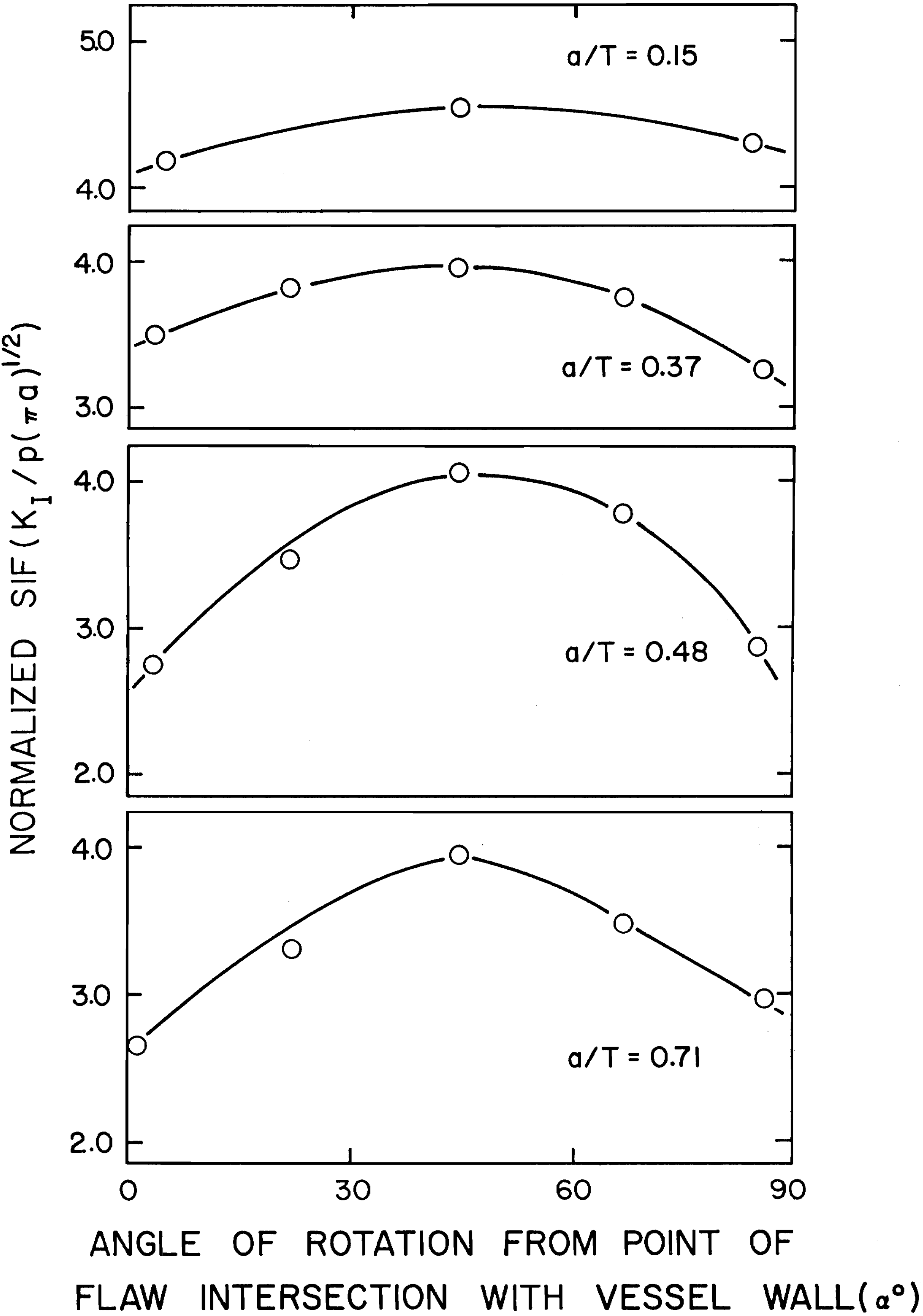

Figure 6.5 SIF Distribution Along the Reactor Vessel Flaw Border.

intensity factor, the value at the crack border midpoint in the present tests was used for comparison with his results. Figure 6.6 shows remarkable agreement with Derby's results except for the shallow flaw where the present stress intensity factor values are 15% below the results of Derby. However, Derby indicated a scatter in his data of about ± 10% in this region.

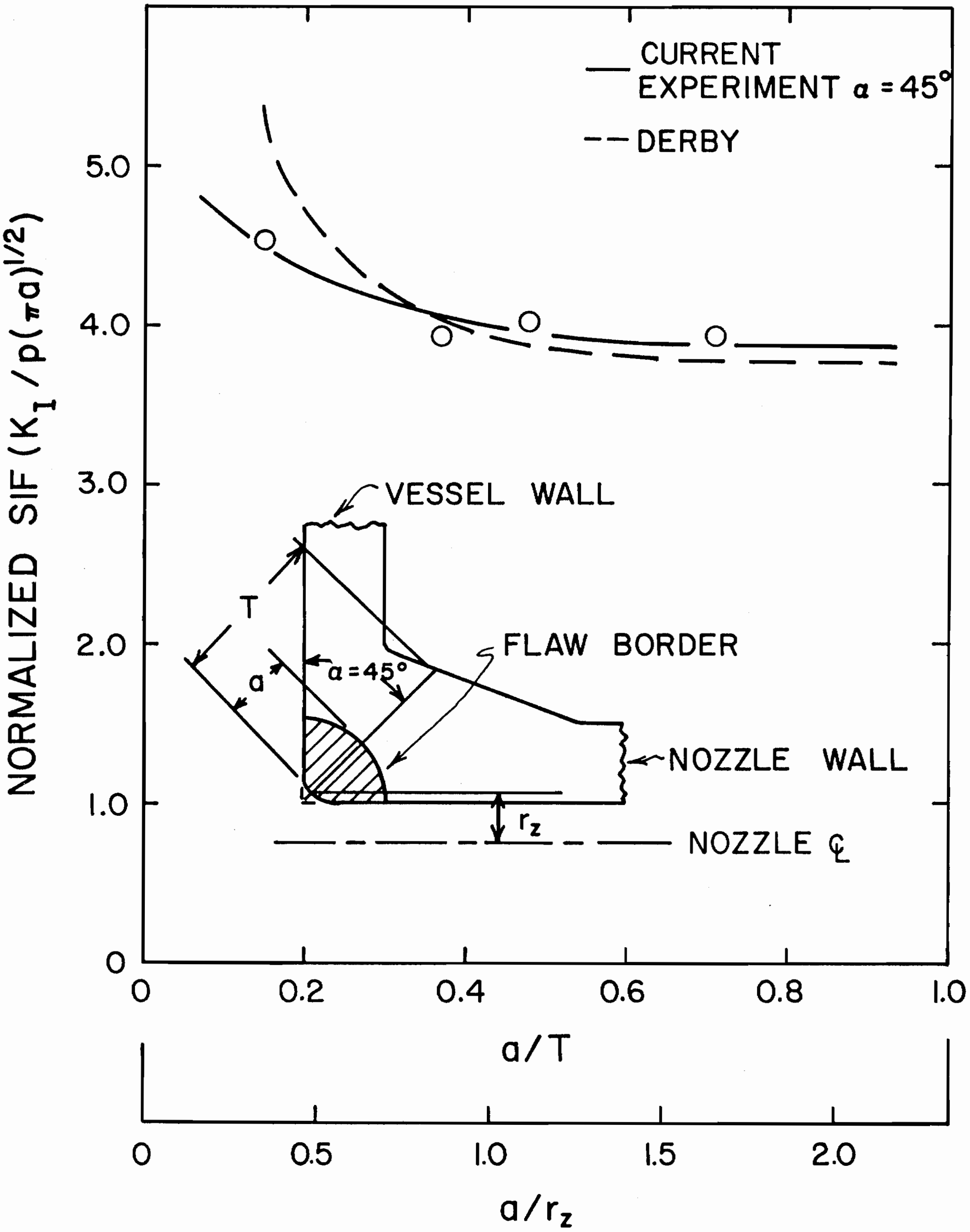

Figure 6.6 Comparison of Results with Derby [60].

VII. APPLICATION TO HOLE CRACKS

Problems associated with flaws emanating from the edge of intersection between a cylindrical hole and a free surface of a finite thickness plate have become those of major technological importance in the aerospace industry. Approximate theories [61-63] have been developed for use by design engineers, but due to the mathematical complexity of the problem, one is led to consider experimental means for obtaining stress intensity factors to assess the accuracy of the approximate theories.

A series of stress freezing photoelastic experiments was designed for the purpose of obtaining values of the stress intensity factor for regions near the intersection of the flaw border and the hole, point H (see Figure 7.1), the intersection of the flaw border and the plate surface, point S, and the intermediate regions IS and IH. The specimens were cast plates of PLM-4B for tests 1-8 and PSM-8F for tests 9-15. Specimen preparation consisted of the following procedure:

i) Drill and ream a circular hole in the center of a plate.

ii) Mount a sharp blade in a special guide and tap a starter flaw into the hole surface-plate surface intersection edge.

iii) For tests 1-8, mount the test specimen in the stress freezing oven, heat to above the critical temperature, grow the crack to the desired size by the application of remote tension, reduce the load to below the threshold value for crack growth, and cool to room temperature. A diagram of the test configuration is presented in Figure 7.2.

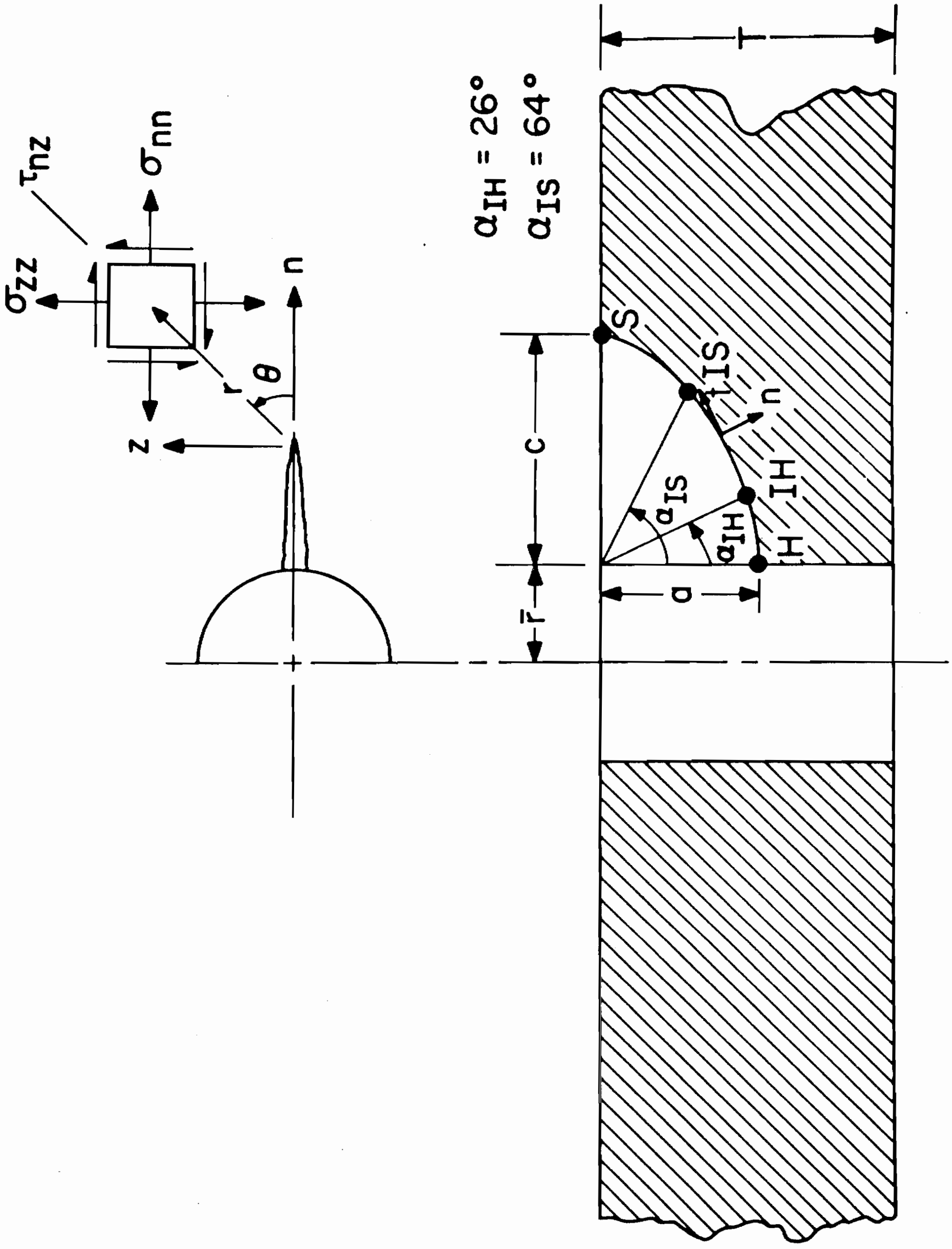

Figure 7.1 Hole Crack Problem Geometry and Notation.

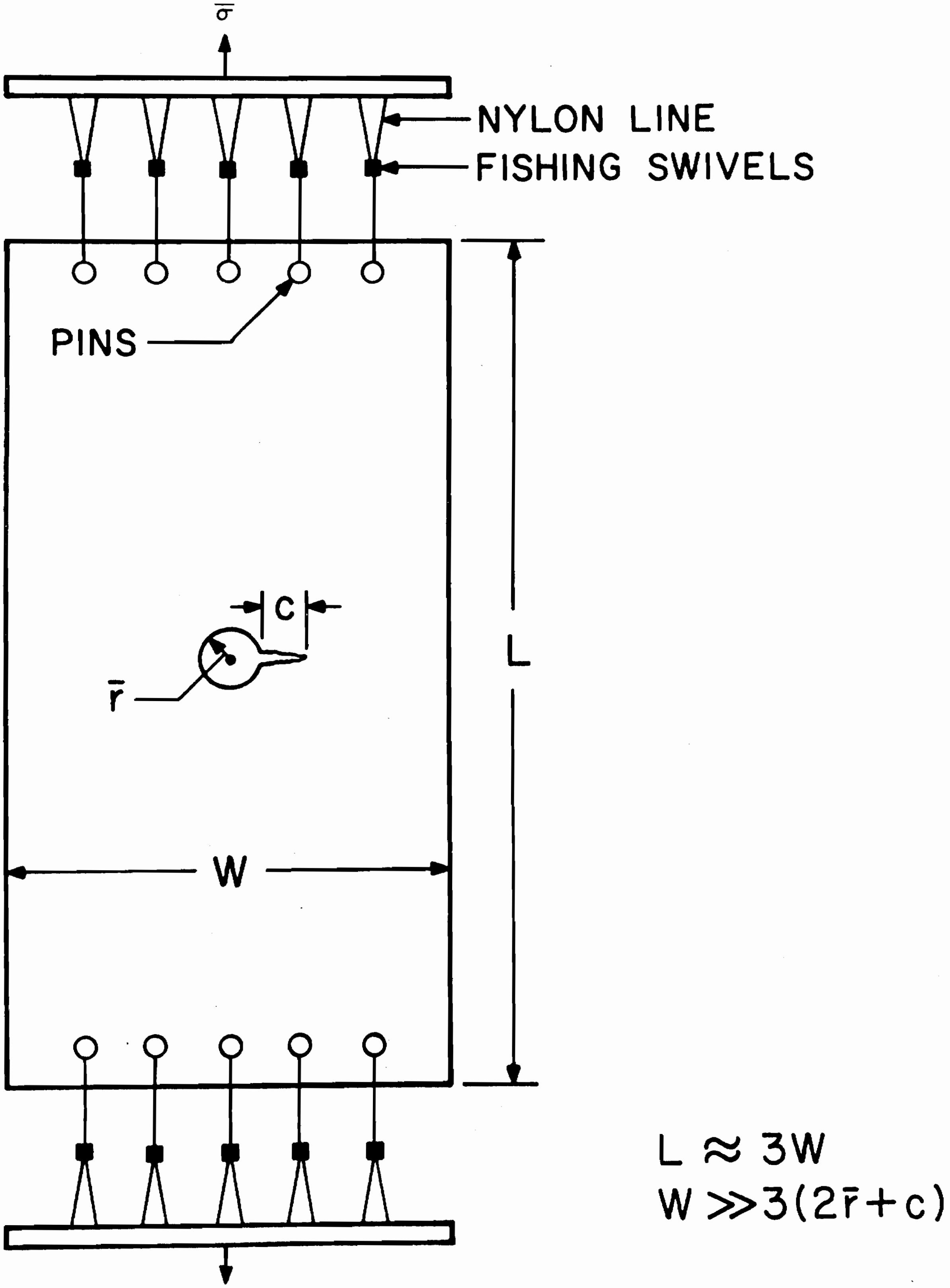

Figure 7.2 Test Configuration for the Hole Crack Experiments.

iv) For tests 9-15, mount the test specimen in the stress freezing oven in a special flexing rig, heat to above the critical temperature, flex the plate to grow the crack to the desired size, and cool to room temperature in a slightly flexed position to avoid crack closure. Remount the specimen in a vertical position for dead weight tension normal to the flaw surface through a string loaded system, heat to above the critical temperature, apply a load, and cool to room temperature.

v) Obtain slices normal to the flaw border and the flaw surfaces in the regions H and S for tests 1-8, and in the regions H, IH, IS and S for tests 9-15.

Observation of the slices in a circular polariscope reveals fringe patterns such as one pictured in Figure 7.3. A set of data from one of the tests is presented in Figure 7.4 showing only the data contained in the singular zone which corresponds to a linear data region on a plot of the normalized apparent stress intensity factor versus the square root of the normalized distance from the crack tip. The results shown in Figure 7.4 may be regarded as typical of all tests.

The results of the first eight tests are summarized in Table 7.1 together with comparisons with the theories of Hall and Finger, Newman, and Shah. Since the first two theories predict only one value of the stress intensity factor, they are compared with the average of the values obtained at points S and H. Agreement was found to be within about 15% for the Hall and Finger theory and to within about 25% for the Newman theory. Individual values of K_I at points S and H were

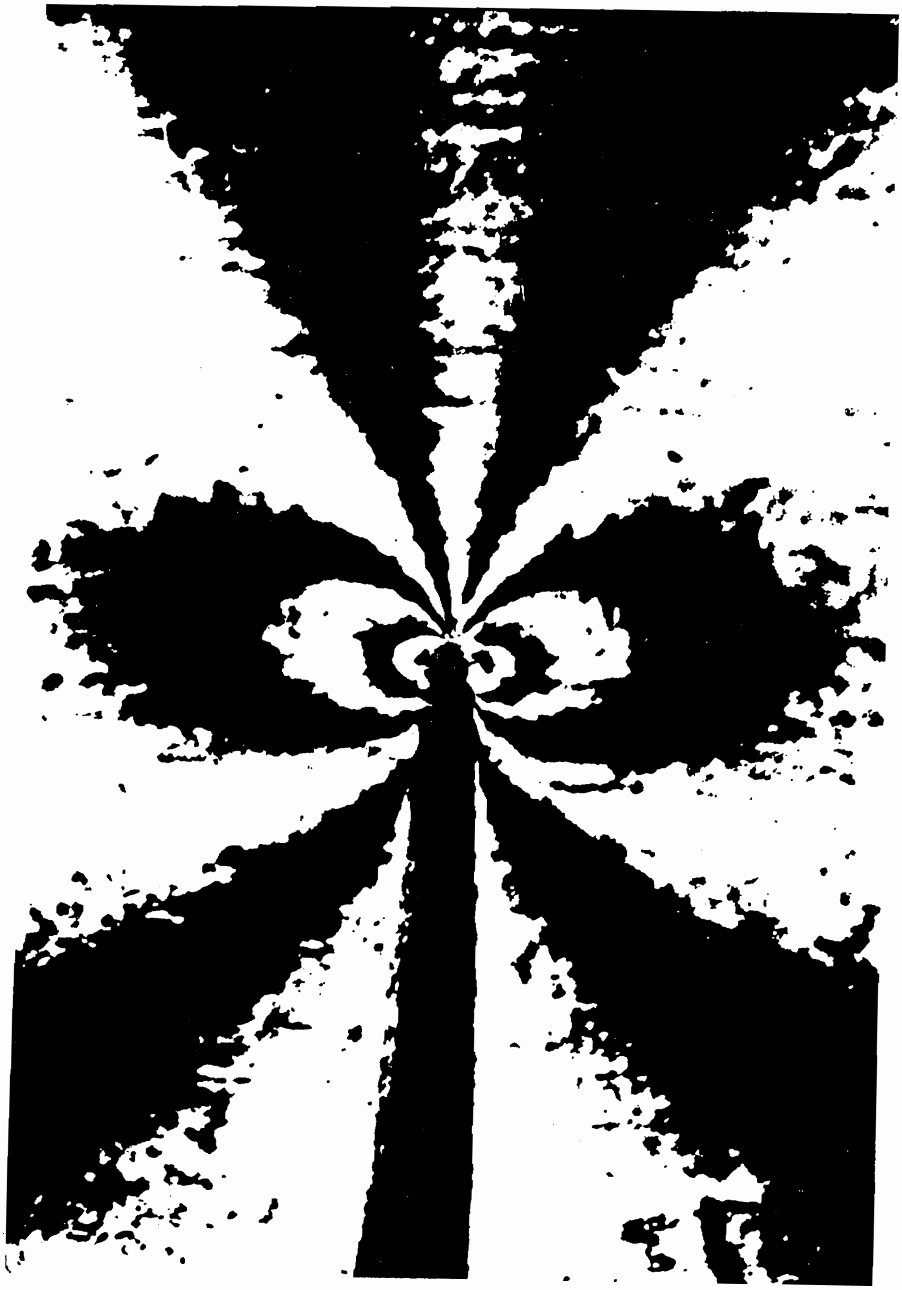

Figure 7.3 Typical Fringe Pattern for the Hole Crack.

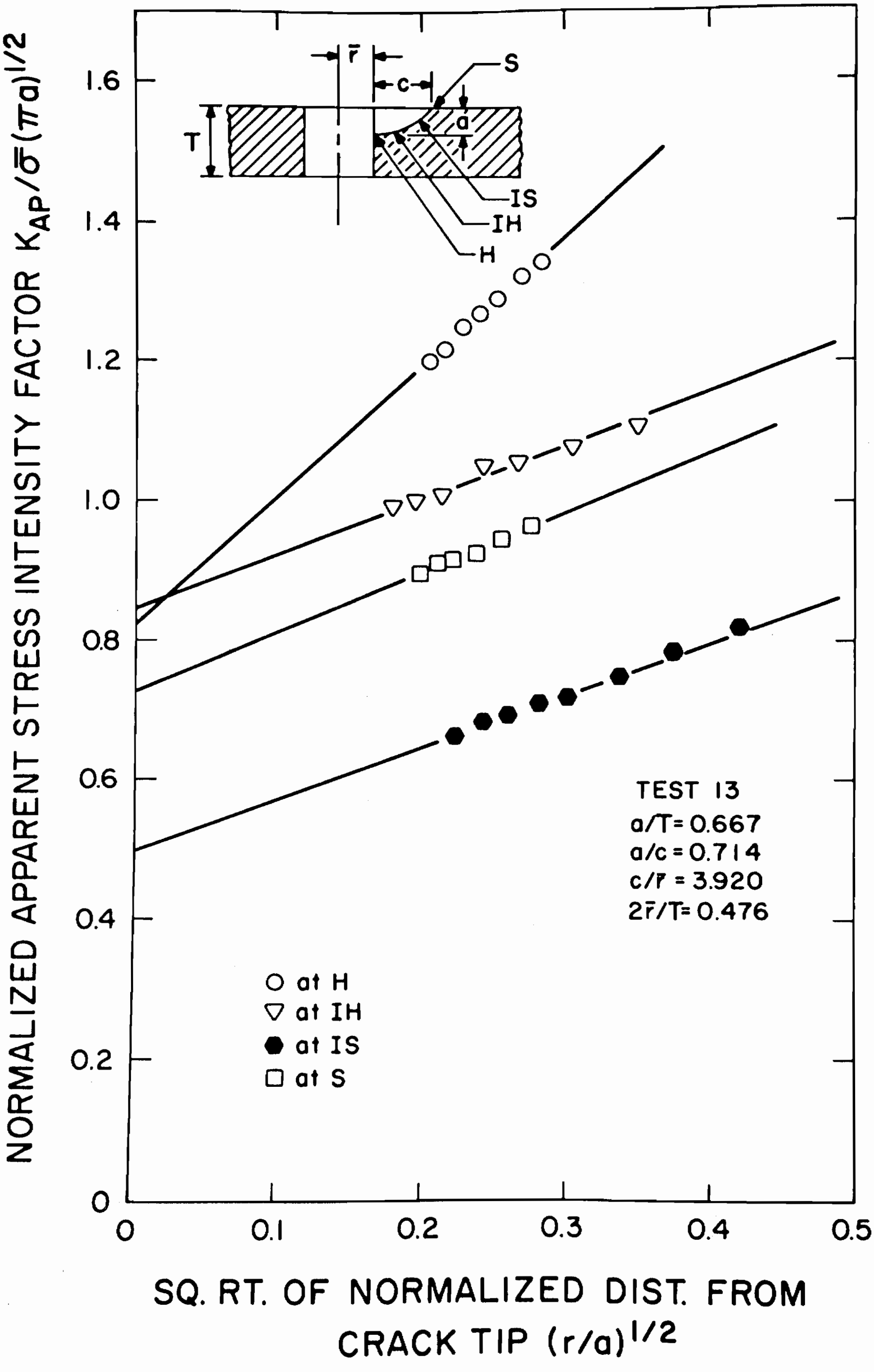

Figure 7.4 Typical Set of Hole Crack Data.

TABLE 7.1

TEST GEOMETRIES AND SIF VALUES FOR HOLE CRACKS--PHASE I

Test Number	1	2	3	4	5	6	7	8
Hole Radius ($\bar{r}$) mm	6.35	6.35	4.83	6.35	4.83	6.35	6.35	4.83
Plate Depth (T) mm	14.70	23.60	19.30	14.50	19.80	13.70	13.50	19.80
Crack Length (c) mm	2.79	3.56	9.65	6.35	7.62	4.06	5.08	7.37
Crack Depth (a) mm	2.54	5.59	8.38	6.86	9.65	6.35	9.91	15.24
Remote Stress ($\bar{\sigma}$) kPa	99.0	108.0	85.0	75.0	81.0	88.0	71.0	62.0
a/T	0.18	0.24	0.43	0.48	0.49	0.46	0.74	0.78
a/c	0.95	1.59	0.86	1.10	1.27	1.55	1.98	2.05
$c/\bar{r}$	0.43	0.56	2.02	0.98	1.60	0.63	0.79	1.56
$2\bar{r}/T$	0.87	0.54	0.49	0.88	0.48	0.94	0.95	0.48
Stress Intensity Factors (Experimental) $\frac{K_I}{\bar{\sigma}(\pi a)^{1/2}}$								
At Point S	1.17	0.99	0.71	0.90	0.86	0.98	0.95	0.72
At Point H	1.91	1.34	1.12	0.89	0.98	1.24	1.08	0.72
Average Points S and H	1.54	1.17	0.92	0.90	0.92	1.11	1.02	0.72
Stress Intensity Factors (Analytical) $\frac{K_I}{\bar{\sigma}(\pi a)^{1/2}}$								
Hall-Finger	1.35	1.05	0.91	1.06	0.82	1.06	0.90	0.72
Newman	1.25	1.04	0.76	0.90	0.75	0.99	0.89	0.69
Shah (at S)	1.31	1.16	0.77	0.97	0.84	1.10	0.96	0.76
Shah (at H)	1.75	1.22	1.36	1.38	1.15	1.22	1.00	0.86

computed from Shah's analysis. Near the plate surface, Shah's results were about 15% above the experimental values for $a/T < 0.25$, and within 10% for $a/t > 0.25$. Shah's values of the stress intensity factor near the hole surface agreed with the experimental results to within 10% for $a/T < 0.25$, and generally within 20% for $a/T > 0.25$.

Results from the latter seven tests are found in Table 7.2. Direct comparisons are made with Shah's theory which appears to overestimate the stress intensity factor near the hole by about 3% to 50%. For the shallower flaws ($a/T < 0.40$) Shah underestimates the value of the stress intensity factor near the surface while for $a/T > 0.40$, the theory produces values higher than those observed in the experiments. There is noted agreement between Shah's analysis and the experimental results at $\alpha = 26°$ from the hole (point IH). From Table 7.2 one can observe that at point IH Shah agrees with the experimental value of K_I to within 10%, except for test 10, the only case where $c \approx \overline{r}$, where it overestimates the experimental result by about 30%.

The Hall and Finger theory is found to agree with the average of the stress intensity values at point H and IH to within 10% except for the very deep flaws (tests 14 and 15) where it underestimates K_I by about 30%. Newman's analysis, intended to yield an average stress intensity factor over the entire flaw border, agreed with the average of the experimental values at points S and H to within 10% for all tests except for test 15 where it overestimates K_I by about 15%.

From the results contained in this chapter it may be concluded that:

TABLE 7.2

TEST GEOMETRIES AND SIF VALUES FOR HOLE CRACKS--PHASE II

Test Number	9	10	11	12	13	14	15
Hole Radius ($\bar{r}$) mm	3.18	6.35	3.18	3.18	3.18	6.35	6.35
Plate Depth (T) mm	13.84	13.03	13.41	13.97	13.34	12.95	13.39
Crack Length (c) mm	5.08	6.35	25.40	19.81	12.45	25.40	38.86
Crack Depth (a) mm	5.08	5.08	7.87	8.64	8.89	11.43	12.45
Remote Stress ($\bar{\sigma}$) kPa	58.59	62.54	51.30	58.26	70.60	43.68	32.47
a/T	0.37	0.39	0.59	0.62	0.67	0.88	0.93
a/c	1.00	0.80	0.31	0.44	0.71	0.45	0.32
c/$\bar{r}$	1.60	1.00	8.00	6.24	3.92	4.00	6.12
2$\bar{r}$/T	0.46	0.98	0.47	0.46	0.48	0.98	0.95
Stress Intensity Factors (Experimental) $\frac{K_I}{\bar{\sigma}(\pi a)^{1/2}}$							
At Point S	0.61	0.70	*	0.67	0.73	0.79	0.57
At Point IS	*	*	*	0.45	0.50	0.92	0.61
At Point IH	0.95	0.93	0.97	0.92	0.85	1.44	1.54
At Point H	1.05	1.25	1.17	0.96	0.83	1.45	1.81
Average Points H and IH	1.00	1.09	1.07	0.94	0.84	1.45	1.68
Average Points S and H	0.83	0.98	*	0.82	0.78	1.12	1.19
Stress Intensity Factors (Analytical) $\frac{K_I}{\bar{\sigma}(\pi a)^{1/2}}$							
Hall-Finger	0.87	1.20	1.10	0.98	0.84	1.10	1.21
Newman	0.77	1.01	0.96	0.84	0.72	1.16	1.35
Shah (at S)	0.84	0.95	0.48	0.54	0.64	0.59	0.48
Shah (at IS)	0.83	0.97	0.84	0.76	0.68	0.93	1.06
Shah (at IH)	0.96	1.28	1.04	0.97	0.89	1.35	1.44
Shah (at H)	1.12	1.63	1.32	1.34	1.25	1.80	1.87

* Insufficient fringes for full spectrum of data.

i) The relative crack depth a/T appears to be the most significant geometric parameter. The second most significant geometric parameter appears to be the crack shape a/c.

ii) The Shah analysis generally provides reasonable values (to within 20%) of the stress intensity factor near points S and H for flaws of $a/c \geq 1.0$ but yields greater errors for lower values of a/c. Excellent agreement is obtained between the experimental results and the values from Shah for the stress intensity factor at the interior region near the hole (point IH) for flaws of $a/c \leq 1.0$.

iii) The Hall and Finger theory agrees with averages of experimental stress intensity factor values to within 15% for shallow to moderately deep flaws ($a/T < 0.80$).

iv) The Newman theory differs from the average experimental stress intensity factor at points S and H by less than 25% for $a/c \geq 1.0$ and generally by less than 15% for lower values of a/c.

VIII. ANALYTICAL FOUNDATIONS FOR THE COMBINED MODE I - MODE II PROBLEM

The technique described for the determination of values of the stress intensity factor has been demonstrated to be a valid procedure through its successful application to several three dimensional problems as described in the preceeding three chapters. The thrust of the previous work was for the solution of problems of Mode I loading. It is now desired to extend the ideas used in the formulation of the analysis described in Chapter II to develop a technique for obtaining values of the Mode I stress intensity factor and the Mode II stress intensity factor from photoelastic data when the problem involves combined loading.

When a cracked body is subjected to mixed mode loadings, one can write, following equation (2.13),

$$\begin{aligned}
\sigma_{nn} &= \frac{K_I}{(2\pi r)^{1/2}} \cos\frac{\theta}{2}\left\{1 - \sin\frac{\theta}{2}\sin\frac{3\theta}{2}\right\} \\
&\quad - \frac{K_{II}}{(2\pi r)^{1/2}} \sin\frac{\theta}{2}\left\{2 + \cos\frac{\theta}{2}\cos\frac{3\theta}{2}\right\} - \overset{\circ}{\sigma}_{nn} \\
\sigma_{zz} &= \frac{K_I}{(2\pi r)^{1/2}} \cos\frac{\theta}{2}\left\{1 + \sin\frac{\theta}{2}\sin\frac{3\theta}{2}\right\} \\
&\quad + \frac{K_{II}}{(2\pi r)^{1/2}} \sin\frac{\theta}{2}\left\{\cos\frac{\theta}{2}\cos\frac{3\theta}{2}\right\} - \overset{\circ}{\sigma}_{zz} \\
\tau_{nz} &= \frac{K_I}{(2\pi r)^{1/2}} \cos\frac{\theta}{2}\left\{\sin\frac{\theta}{2}\cos\frac{3\theta}{2}\right\} \\
&\quad + \frac{K_{II}}{(2\pi r)^{1/2}} \cos\frac{\theta}{2}\left\{1 - \sin\frac{\theta}{2}\sin\frac{3\theta}{2}\right\} - \overset{\circ}{\tau}_{nz}
\end{aligned} \tag{8.1}$$

where the notation again refers to Figure 2.6 for the problem at hand. In the three dimensional problem, the values of the stress intensity factors, K_I and K_{II}, will, in general, vary along the crack border. The terms $\overset{o}{\sigma}_{nn}$, $\overset{o}{\sigma}_{zz}$ and $\overset{o}{\tau}_{nz}$ are added to the singular expressions to account for the contribution of the regular part of the stress field to the components of stress near the crack tip. Although treated as constants in a plane perpendicular to any point along the flaw border, the values of these terms will also usually vary as one moves along the crack border.

If we use the above equations to obtain an expression for the maximum shear stress in the nz plane (as before with equation (2.14)), we can expand this expression, and truncating to the same order as the crack tip stress field equations (8.1), write

$$\tau_{max} = \frac{A}{r^{1/2}} + B \tag{8.2}$$

The coefficients of the above expansion reduce to

$$\begin{aligned} A &= \left\{\frac{1}{8\pi}\left[(K_I \sin\theta + 2\,K_{II}\cos\theta)^2 + (K_{II}\sin\theta)^2\right]\right\}^{1/2} \\ B &= B(K_I, K_{II}, \theta, \overset{o}{\sigma}_{nn}, \overset{o}{\sigma}_{zz}, \overset{o}{\tau}_{nz}) \end{aligned} \tag{8.3}$$

It is important to note here that, in contrast to the pure Mode I case, no value for θ has been specified in equations (8.2) and (8.3).

Now, in general, the effects of the regular stress field components involve both a folding and a change in eccentricity of the fringe loops [17]. If folding occurs, Θ_m, the angle along which the distance to a fringe from the crack tip is greatest, will vary with the fringe order n' (see Figure 8.1). In this case, one must plot the angle Θ_m versus the normalized distance r/a and extrapolate to the crack tip (r/a = 0) in order to obtain $\overset{o}{\Theta}_m$, the value of Θ_m at the crack tip and that which is associated with K_I and K_{II}. Observation of a typical fringe pattern as shown in Figure 8.2 indicates that in the vicinity of the crack tip, which corresponds to the region in which the photoelastic data is gathered, the angle Θ_m approaches a constant. This trend is shown qualitatively in Figure 8.1. It may be noted, however, that this trend is not a prerequisite to the application of the technique.

Upon computing

$$\lim_{\substack{r\to 0 \\ \Theta_m \to \overset{o}{\Theta}_m}} \left\{ (8\pi r)^{1/2} \frac{\partial \tau_{max}}{\partial \theta} (K_I, K_{II}, r, \theta, \overset{o}{\sigma}_{nn}, \overset{o}{\sigma}_{zz}, \overset{o}{\tau}_{nz}) \right\} = 0 \qquad (8.4)$$

one obtains the relation

$$\left(\frac{K_{II}}{K_I}\right)^2 - \frac{4}{3}\left(\frac{K_{II}}{K_I}\right) \cot 2\overset{o}{\Theta}_m - \frac{1}{3} = 0 \qquad (8.5)$$

By inserting the measured value of $\overset{o}{\Theta}_m$ into equation (8.5), the quantity (K_{II}/K_I) can be computed. Then, by defining a combined mode apparent stress intensity factor,

$$K_{AP}^{*} = \tau_{max} \, (8\pi r)^{1/2} \qquad (8.6)$$

and using the stress optic law (equation (2.6)) to obtain the values of τ_{max}, we can solve for the individual values of the normalized Mode I and Mode II stress intensity factors, $K_I/\bar{\sigma}(\pi a)^{1/2}$ and $K_{II}/\bar{\sigma}(\pi a)^{1/2}$.

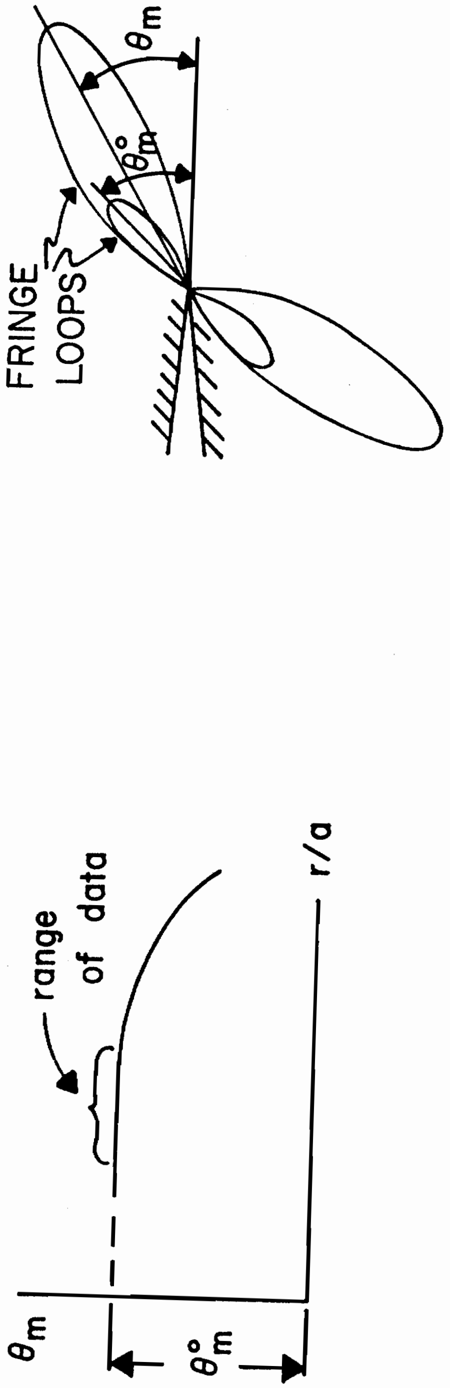

Figure 8.1 Stress Fringe Notation for the General Mode I - Mode II Problem.

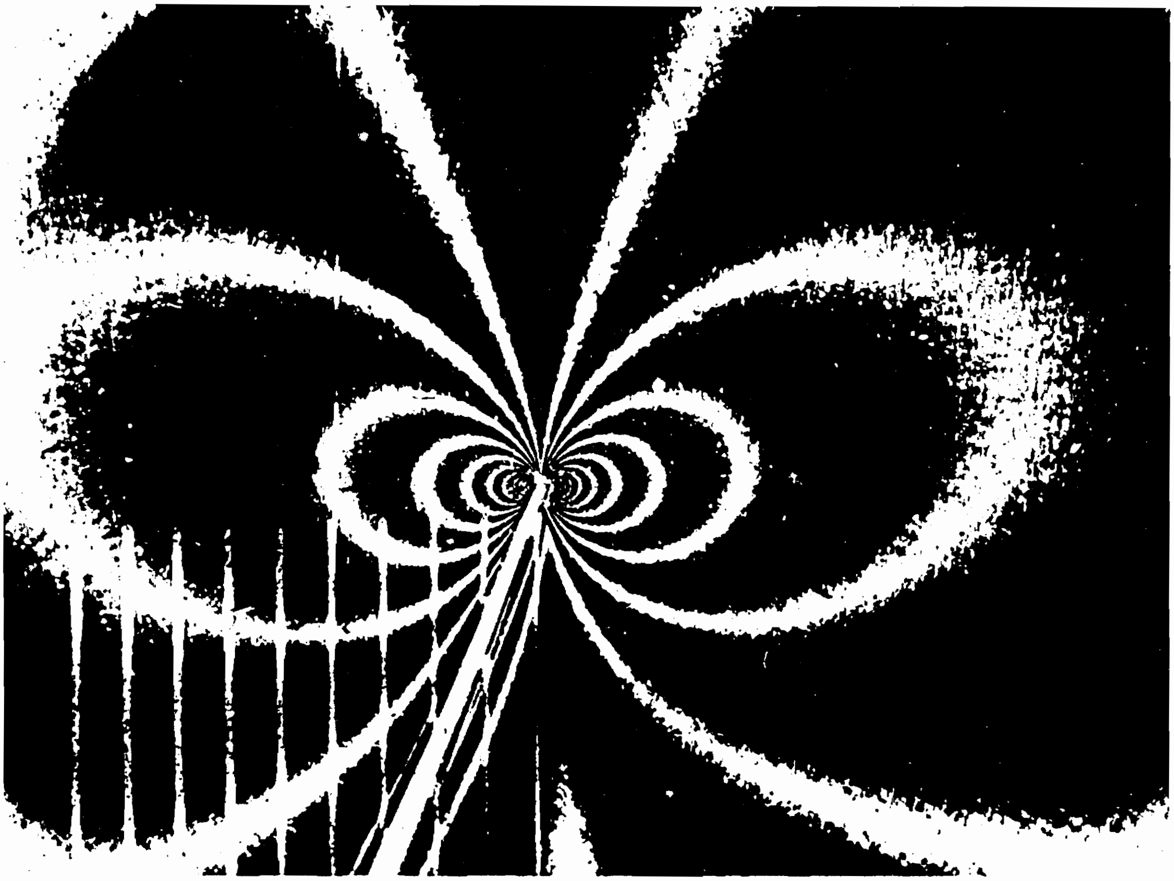

Figure 8.2 Fringe Pattern for Combined Mode I - Mode II Loading.

In order to do this we obtain the normalized combined mode stress intensity factor

$$\frac{K^*}{\bar{\sigma}(\pi a)^{1/2}} = \left\{ \left[\frac{K_I}{\bar{\sigma}(\pi a)^{1/2}} \sin \theta_m^\circ + 2 \frac{K_{II}}{\bar{\sigma}(\pi a)^{1/2}} \cos \theta_m^\circ \right]^2 + \left[\frac{K_{II}}{\bar{\sigma}(\pi a)^{1/2}} \sin \theta_m^\circ \right]^2 \right\}^{1/2} \tag{8.7}$$

by plotting a normalized combined mode apparent stress intensity factor versus the square root of the normalized distance from the crack tip, $K^*_{AP}/\bar{\sigma}(\pi a)^{1/2}$ versus $(r/a)^{1/2}$, identifying the linear region of the plot, which corresponds to the singular zone, and extrapolating to an $(r/a)^{1/2} = 0$, as was done for the Mode I case.

This technique is utilized in the analysis of the problem of the following chapter.

IX. APPLICATION TO FASTENER LOADED HOLE CRACKS

The problem of cracks emanating from open holes in plates loaded by remote tension was addressed in Chapter VI. As mentioned at that time, the three dimensional complexities of the problem have prevented the accomplishment of extensive analytical work. The determination of stress intensity factors along the border of a flaw emanating from the corner formed by the intersection of the surface of a flat plate with the boundary of a neat fit, rigid pin loaded hole presents additional difficulties. Any analytical work undertaken, even that of an approximate nature, requires first the solution to the contact problem of the pin loaded hole and then the analysis of the crack problem. Only one such combined attempt has been reported in the literature [63].

A series of stress freezing photoelastic experiments were conducted to investigate this important technological problem. Models were constructed from cast plates of PSM-8F. The model making procedure consisted of:

i) Drill and ream a circular hole in the center of a plate.

ii) Tap in a starter crack at the hole-plate surface interface.

iii) Insert a neat fit aluminum pin into the hole and mount the model in a dead loading rig in the stress freezing oven.

iv) Heat to above the critical temperature, apply remote tension normal to the flaw surface, grow the natural crack to the desired size, remove the load and cool to room temperature.

v) Heat to above the critical temperature, apply a live load through the pin and cool to room temperature.

vi) Obtain appropriate slices as indicated in Figure 9.1.

The geometries tested are shown in the upper part of Table 9.1.

Fringe patterns typical of those observed when viewing the slices in a circular polariscope are presented in Figure 9.2. The data extracted from fringe patterns such as those in Figure 9.2 is shown in Figure 9.3. Results are tabulated in the middle of Table 9.1.

The dysymmetry of the fringes around the crack plane in Figure 9.2a reveals the presence of mixed mode behavior near point S while the symmetric fringe geometry in Figure 9.2b reveals only Mode I loading near point H. Values of the Mode II stress intensity factor K_{II} were found to be from 11% to 22% of the K_I values as noted in Table 9.1.

Values of the Mode I stress intensity factor at point H were significantly larger than values of K_I at point S for all geometries tested. Tests 4 and 5 were for nearly identical geometries, and results are seen to differ by about 10%.

Chapter 7 contains tests on geometries similar to those of tests 1P, 6P and 7P of this chapter. Comparing the results of these pin loaded hole tests with the experiments of remote tensile loading and an open hole, it was found that at point S, K_I for the pin loaded tests was about two to four times the value of the stress intensity factor for the open hole; at point H, the stress intensity factor for the pin loaded tests was two to five times the value of K_I without the pin.

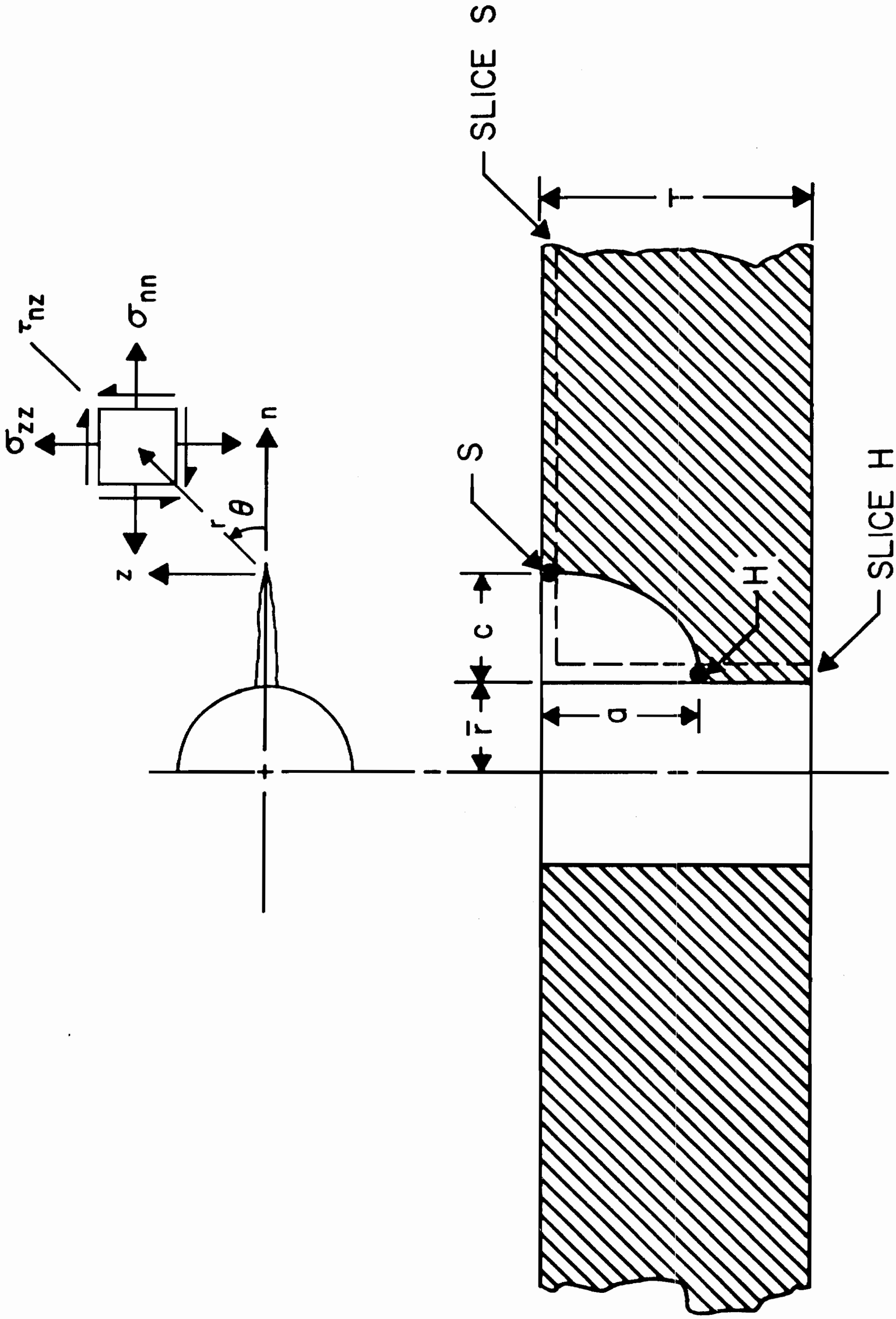

Figure 9.1 Pin Loaded Hole Crack Geometry and Notation.

TABLE 9.1

TEST GEOMETRIES AND SIF VALUES FOR THE PIN LOADED HOLE CRACKS

Test Number	1P	2P	3P	4P	5P	6P	7P	8P
Hole Radius ($\bar{r}$) mm	6.67	6.67	3.18	3.18	3.18	6.67	3.18	6.67
Plate Depth (T) mm	13.21	12.95	13.21	12.95	13.46	12.85	13.72	12.95
Crack Length (c) mm	2.29	3.30	2.79	2.79	2.79	4.57	5.33	6.60
Crack Depth (a) mm	2.54	3.56	4.83	5.59	5.84	7.11	10.92	11.43
Bearing Stress (σ_b) kPa	265.	270.	557.	568.	547.	273.	536.	193.
a/T	0.19	0.28	0.37	0.43	0.43	0.55	0.80	0.88
a/c	1.11	1.08	1.69	2.00	2.08	1.56	2.04	1.73
c/$\bar{r}$	0.34	0.50	0.88	0.88	0.88	0.69	1.68	0.99
2$\bar{r}$/T	1.01	1.03	0.48	0.49	0.47	1.04	0.46	1.03
Stress Intensity Factors at S (Experiments)								
$\frac{K_I}{\sigma_b(\pi a)^{1/2}}$	0.181	0.129	0.165	0.156	0.132	0.181	0.091	0.211
$\frac{K_{II}}{\sigma_b(\pi a)^{1/2}}$	0.020	0.029	0.034	0.026	*	0.030	0.017	0.036
Stress Intensity Factors at H (Experiments)								
$\frac{K_I}{\sigma_b(\pi a)^{1/2}}$	0.376	0.386	0.243	0.225	0.205	0.215	0.117	0.285
Stress Intensity Factors (Shah Theory)								
(At S) $\frac{K_I}{\sigma_b(\pi a)^{1/2}}$	0.355	0.289	0.198	0.190	0.188	0.237	0.123	0.182
(At H) $\frac{K_I}{\sigma_b(\pi a)^{1/2}}$	0.474	0.442	0.289	0.240	0.256	0.312	0.254	0.305

* Tests 4P and 5P were intended as approximate replications. However, the crack growth in 5P was small and at an angle to the initial flaw, invalidating the data for K_{II}.

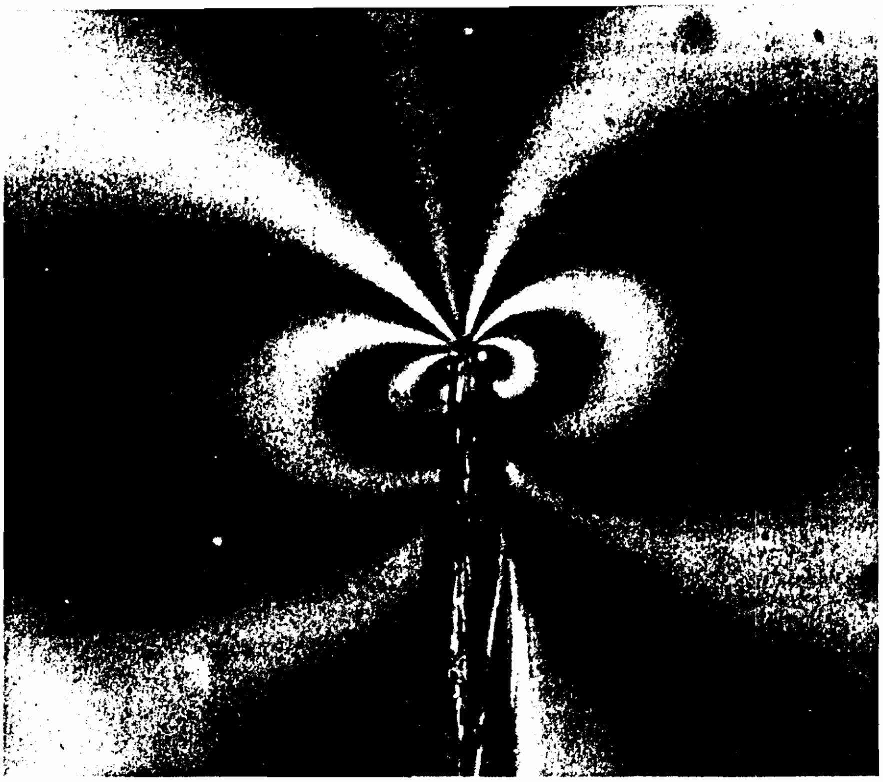

Figure 9.2a Typical Fringe Pattern for Pin Loaded Hole Crack at Point S.

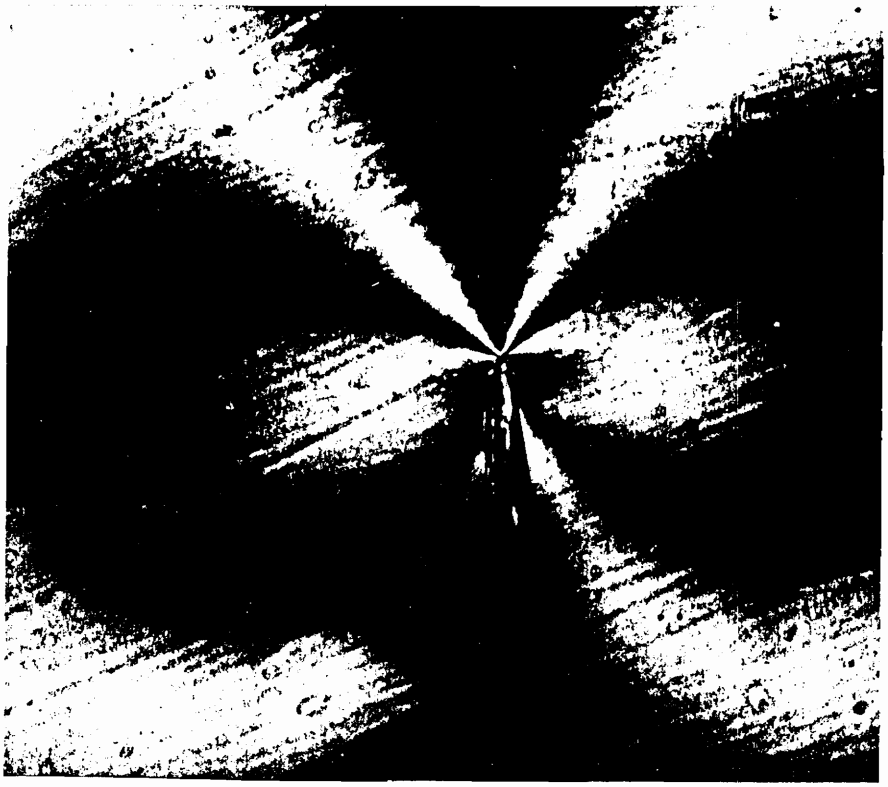

Figure 9.2b Typical Fringe Pattern for Pin Loaded Hole Crack at Point H.

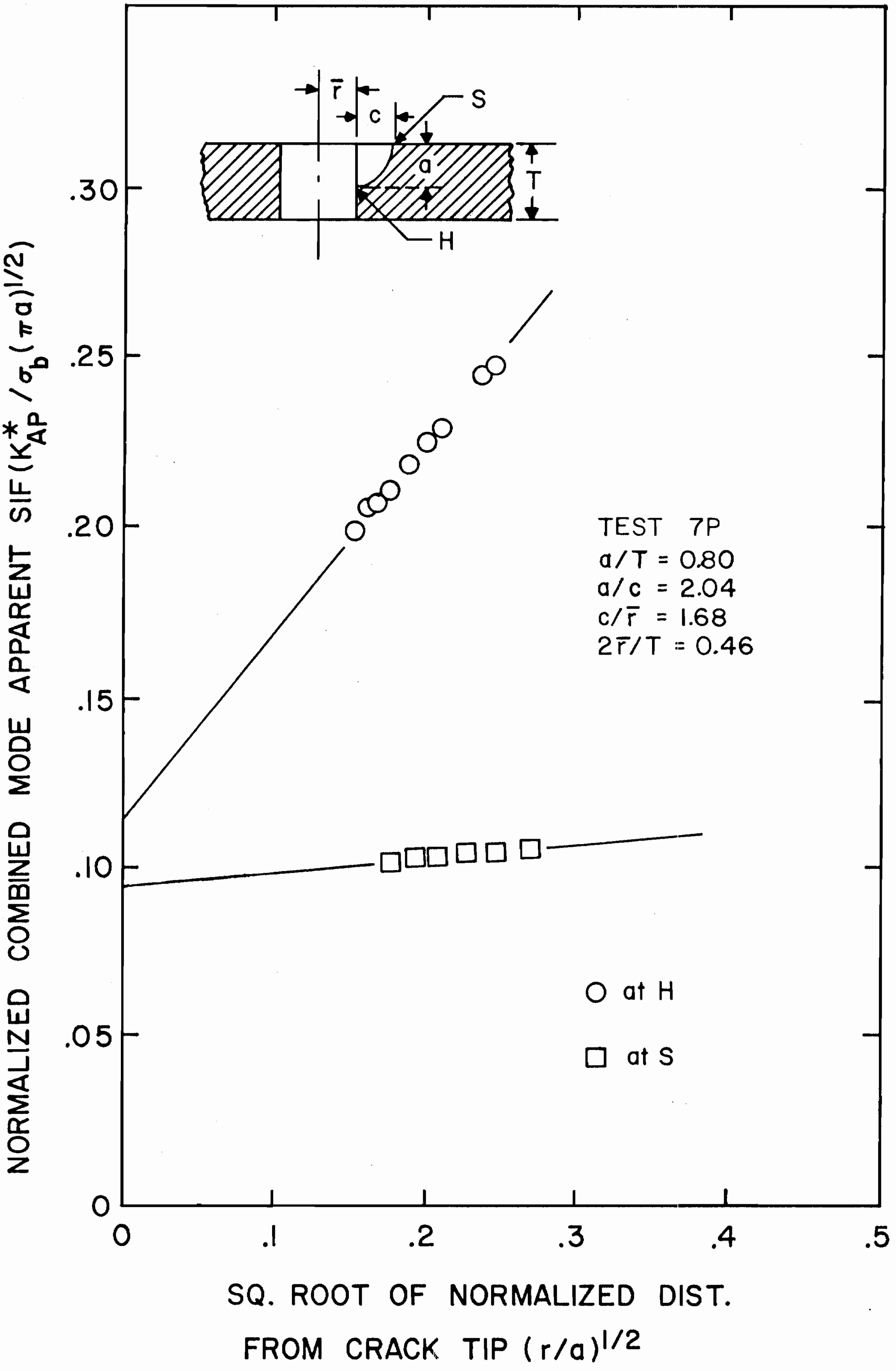

Figure 9.3 Typical Set of Data for the Pin Loaded Hole Crack Experiments.

Comparisons are made with the approximate theory constructed by Shah in Table 9.1. In making the comparisons, results from the analytical work were computed at the midthickness of each specimen slice. At point S, Shah overestimated K_I by 20% to 125% except for the deep flaw in test 8 ($a/T = 0.88$) where the experimental result was greater than the value determined from the analytical work. At point H, Shah's theory again overestimates the experimental Mode I stress intensity factor values by 10% to 110%. However, the larger discrepancies occurred only for the deep flaws ($a/T > 0.5$). Shah did not present results for Mode II stress intensity factors for the problem.

On the basis of the studies described in this chapter it is concluded that:

i) Stress intensity factors for cracks emanating from neat fit, rigid pin loaded holes are several hundred percent higher than those obtained for remote tensile loading of open holes.

ii) The available design theory generally overestimates the stress intensity factors for the pin loaded holes with cracks.

iii) Mixed mode effects are present near point S.

X. SUMMARY AND CONCLUSIONS

Solutions providing values of the stress intensity factor for finite three dimensional cracked body problems are required for the design process. Although solutions to several such problems exist, most of these involve approximations or are obtained through numerical techniques, and thus their accuracy must be assessed.

An experimental technique is described involving stress freezing photoelasticity to obtain information concerning the stress field around a crack tip which allows the determination of the stress intensity factor. The major advantages of the method over previous photoelastic techniques are that stress separation of the photoelastic data is not required and the approach utilizes the full field of photoelastic data in a least squares analysis for the evaluation of stress intensity factor values.

The limitations of the method are that the materials used for the experimental models are incompressible above the critical temperature and that a linear data region must be located on a graph of the normalized apparent stress intensity factor versus the square root of the normalized distance from the crack tip for the stress intensity factor determination. The problem of the elevated value of Poisson's ratio can be accounted for as discussed in Chapter 3. The linear zone on the apparent stress intensity factor graph was found to exist for all problems studied to date.

The technique is applied to several three dimensional cracked body problems of current technological interest. Comparisons are made between the experimentally determined stress intensity factors and values obtained from appropriate analytical work.

Replications of identical test geometries indicate a scatter in the results of less than ± 5%.

It is concluded that, with adequate replications for data assessment and proper accounting of the influence of the elevated value of Poisson's ratio, a reasonable degree of accuracy can be achieved so that the method may be regarded as a viable means for independent determination of values of the stress intensity factor in three dimensional cracked body problems.

REFERENCES

[1] Griffith, A. A., "The Phenomenon of Rupture and Flow in Solids", *Phil. Trans. of the Royal Society of London*, Vol. 221, pp. 163-198, 1921.

[2] Irwin, G. R., "Fracture Dynamics", *Fracturing of Metals*, pp. 147-166, 1948.

[3] Irwin, G. R., "Onset of Fast Crack Propagation in High Strength Steel and Aluminum Alloys", *Proceedings of the 1955 Sangamore Conference on Ordinance Materials*, Vol. II, 1956.

[4] Paris, P. C., "A Rational Analytic Theory of Fatigue", *The Trend in Engineering*, January 1961.

[5] Sih, G. C., *Handbook of Stress Intensity Factors for Researchers and Engineers*, Institute of Fracture and Solid Mechanics, Lehigh University, Bethlehem, Pa., 1973.

[6] Tada, H., Paris, P. C. and Irwin, G. R., *The Stress Analysis of Cracks Handbook*, Del Research Corp., Providence, R. I., 1973.

[7] Rooke, D. P. and Cartwright, D. J., *Compendium of Stress Intensity Factors*, Pendragon House, Palo Alto, Calif., 1976.

[8] Sneddon, I. N., "The Distribution of Stress in the Neighborhood of a Crack in an Elastic Solid", *Proceedings of the Royal Society, Series A*, Vol. 187, pp. 229-260, 1946.

[9] Green, A. E. and Sneddon, I. N., "The Distribution of Stress in the Neighborhood of a Flat Elliptical Crack in an Elastic Solid", *Proceedings of the Cambridge Philosophical Society*, Vol. 46, pp. 159-163, 1950.

[10] Irwin, G. R., "Discussion", *Proceedings of the Society for Experimental Stress Analysis*, Vol. 16, No. 1, pp. 92-96, 1958.

[11] Post, D., "Photoelastic Stress Analysis for an Edge Crack in a Tensile Field", *Proceedings of the Society for Experimental Stress Analysis*, Vol. 12, No. 1, pp. 99-116, 1954.

[12] Wells, A. A. and Post, D., "The Dynamic Stress Distribution Surrounding a Running Crack--A Photoelastic Analysis", *Proceedings of the Society for Experimental Stress Analysis*, Vol. 16, No. 1, pp. 69-92, 1958.

[13] Marloff, R. H., Leven, M. M., Johnson, R. L. and Ringler, T. N., "Photoelastic Determination of Stress Intensity Factors", Experimental Mechanics, Vol. 11, No. 12, pp. 529-539, 1971.

[14] Smith, D. G. and Smith, C. W., "A Photoelastic Evaluation of the Influence of Closure and Other Effects upon the Local Bending Stresses in Cracked Plates", International Journal of Fracture Mechanics, Vol. 6, No. 3, pp. 303-318, 1970.

[15] Smith, D. G. and Smith, C. W., "Influence of Precatastrophic Extension and Other Effects on Local Stresses in Cracked Plates under Bending Fields", Experimental Mechanics, Vol. 11, No. 9, pp. 394-401, 1971.

[16] Marrs, G. R. and Smith, C. W., "A Study of Local Stresses Near Surface Flaws in Bending Fields", Stress Analysis and Growth of Cracks, ASTM STP 513, pp. 22-36, 1972.

[17] Schroedl, M. A., McGowan, J. J. and Smith, C. W., "An Assessment of Factors Influencing Data Obtained by the Photoelastic Stress Freezing Technique for Stress Fields Near Crack Tips", Journal of Engineering Fracture Mechanics, Vol. 4, No. 4, 1972.

[18] Bradley, W. B. and Kobayashi, A. S., "An Investigation of Propagating Cracks by Dynamic Photoelasticity", Experimental Mechanics, Vol. 10, No. 3, pp. 106-113, 1970.

[19] Bradley, W. B. and Kobayashi, A. S., "Fracture Dynamics--A Photoelastic Investigation", Journal of Engineering Fracture Mechanics, Vol. 3, No. 3, pp. 317-332, 1971.

[20] Kobayashi, A. S., Wade, B. G., Bradley, W. B. and Chiu, S. T., "Crack Branching in Homalite-100 Sheets", TR-13, Department of Mechanical Engineering, University of Washington, Seattle, Washington, June 1972.

[21] Kobayashi, A. S. and Wade, B. G., "Crack Propagation and Arrest in Impacted Plates", TR-14, Department of Mechanical Engineering, University of Washington, Seattle, Washington, July 1972.

[22] Schroedl, M. A. and Smith, C. W., "Local Stresses Near Deep Surface Flaws Under Cylindrical Bending Fields", Progress in Flaw Growth and Fracture Toughness Testing, ASTM STP 536, pp. 45-63, 1973.

[23] Schroedl, M. A., McGowan, J. J. and Smith, C. W., "Determination of Stress Intensity Factors from Photoelastic Data with Application to Surface Flaw Problems", Experimental Mechanics, Vol. 14, No. 10, pp. 392-399, 1974.

[24] Schroedl, M. A. and Smith, C. W., "Influence of Three Dimensional Effects on the Stress Intensity Factors of Compact Tension Specimens", Fracture Analysis, ASTM STP 560, pp. 69-80, 1974.

[25] Harms, A. E. and Smith, C. W., "Stress Intensity Factors in Long Deep Surface Flaws in Plate Under Extensional Fields", Proceedings of the Tenth Anniversary Meeting of the Society for Engineering Science, 1974.

[26] Jolles, M., McGowan, J. J. and Smith, C. W., "Finite Width Effects on Stress Intensities for Surface Flaws Using a Hybrid Computer Assisted Photoelastic Analysis", Proceedings of the Eleventh Annual Meeting of the Society for Engineering Science, pp. 320-321, 1974.

[27] Jolles, M., McGowan, J. J. and Smith, C. W., "Experimental Determination of Side Boundary Effects on Stress Intensity Factors in Surface Flaws", Journal of Engineering Materials and Technology, Vol. 97, No. 1, pp. 45-51, 1975.

[28] Jolles, M., McGowan, J. J. and Smith, C. W., "Use of a Hybrid Computer Assisted Photoelastic Technique for Stress Intensity Determination in Three Dimensional Problems", Computational Fracture Mechanics (ASME Special Publication), pp. 83-102, 1975.

[29] Jolles, M., McGowan, J. J. and Smith, C. W., "Stress Intensities for Cracks Emanating from Holes in Finite Thickness Plates", Proceedings of the Twelfth Annual Meeting of the Society for Engineering Science, pp. 353-362, 1975.

[30] Jolles, M. and Smith, C. W., "Stress Intensities in Deep Surface Flaws in Plates Under Mode I Loading", Developments in Theoretical and Applied Mechanics (Southeast Conference on Theoretical and Applied Mechanics), pp. 151-161, 1976.

[31] Jolles, M., McGowan, J. J. and Smith, C. W., "Effects of Artificial Cracks and Poisson's Ratio Upon Photoelastic Stress Intensity Determination", Experimental Mechanics, Vol. 16, No. 5, pp. 188-193, 1976.

[32] Jolles, M., Peters, W. H. and Smith, C. W., "Stress Intensity Determination in Three Dimensional Problems by the Photoelastic Method", Proceedings of the Second International Conference on the Mechanical Behavior of Materials, 1976.

[33] Jolles, M., Peters, W. H. and Smith, C. W., "Stress Intensities for Cracks Emanating from Fastener Loaded Holes", Proceedings of the Tenth National Symposium on Fracture Mechanics, 1976.

[34] Jolles, M., Hu, T. and Smith, C. W., "Stress Intensities for Low Aspect Ratio Surface Flaws in Pressurized Thick Walled Tubes", Experimental Mechanics (In Press).

[35] Jolles, M., Peters, W. H. and Smith, C. W., "Stress Intensities in Flawed Pressure Vessels", Proceedings of the Third International Conference on Pressure Vessels and Piping Technology (In Press).

[36] Westergaard, H. M., "Bearing Pressures on Cracks", Journal of Applied Mechanics, Vol. 4, 1939.

[37] Kassir, M. and Sih, G. C., "Three Dimensional Stress Distribution Around an Elliptical Crack Under Arbitrary Loadings", Journal of Applied Mechanics, Vol. 33, No. 3, pp. 601-611, 1966.

[38] Sih, G. C. and Liebowitz, H., "Mathematical Theories of Brittle Fracture", Fracture (Vol. II, Mathematical Fundamentals), pp. 68-188, 1968.

[39] Oppel, G., "Photoelastic Investigation of Three-Dimensional Stress and Strain Conditions", NACA TM 824 (Translation by J. Vanier), 1937.

[40] Gross, B. and Srawley, J. E., "Stress Intensity Factors for Single Edge Notch Specimens in Bending or Combined Bending and Tension by Boundary Collocation of a Stress Function", NASA TN-D-2603, 1965.

[41] Cruse, T. A., "Lateral Constraint in a Cracked Three Dimensional Elastic Body", International Journal of Fracture Mechanics, Vol. 6, No. 3, pp. 326-328, 1970.

[42] Brown, W. F. and Srawley, J. E., "Fracture Toughness Testing", Fracture Toughness Testing and Its Applications, ASTM STP 381, pp. 133-196, 1964.

[43] Irwin, G. R., "Measurement Challenges in Fracture Mechanics", William Murray Lecture, SESA Fall Meeting, 1973.

[44] Rice, J. R., "A Path Independent Integral and the Approximate Analysis of Strain Concentration by Notches and Cracks", Journal of Applied Mechanics, pp. 379-386, 1968.

[45] Paris, P. C. and Sih, G. C., "Stress Analysis of Cracks", Fracture Toughness Testing and Its Applications, ASTM STP 381, pp. 30-81, 1964.

[46] Dixon, J. R. and Strannigan, J. S., "A Photoelastic Investigation of the Stress Distribution in Uniaxially Loaded Thick Plates Containing Slits", NEL-288, National Engineering Laboratory, Scotland, 1967.

[47] Gross, B. E. and Mendelson, A., "Plane Elasto-static Analysis of V-Notched Plates", International Journal of Fracture Mechanics, Vol. 8, No. 3, pp. 267-376, 1972.

[48] Schroedl, M. A. and Smith, C. W., "A Study of Near and Far Field Effects in Photoelastic Stress Intensity Determination", Journal of Engineering Fracture Mechanics, Vol. 7, No. 2, pp. 341-356, 1975.

[49] Savin, C. N., Stress Concentrations Around Holes, Pergamon Press, pp. 9-14, 1961.

[50] Irwin, G. R., "Crack Extension Force for a Part Through Crack in a Plate", Journal of Applied Mechanics, Vol. 29, No. 4, pp. 651-654, 1962.

[51] Green, A. E. and Sneddon, I. N., "The Distribution of Stress in the Neighborhood of a Flat Elliptical Crack in an Elastic Solid", Proceedings of the Cambridge Philosophical Society, Vol. 46, pp. 159-163, 1950.

[52] Swedlow, J. E., (Editor), The Surface Crack: Physical Problems and Computational Solutions (ASME Special Publication), 1972.

[53] Smith, F. W., "Stress Intensity Factors for a Surface Flawed Fracture Specimen", TR-1, Department of Mechanical Engineering, Colorado State University, Ft. Collins, Colorado, Sept. 1971.

[54] Shah, R. C. and Kobayashi, A. S., "Stress Intensity Factors for an Elliptical Crack Approaching the Surface of a Semi-infinite Solid", International Journal of Fracture, Vol. 9, No. 2, pp. 133-146, 1973.

[55] Rice, J. R. and Levy, N., "The Part Through Surface Crack in an Elastic Plate", Journal of Applied Mechanics, Vol. 39, No. 1, pp. 185-194, 1972.

[56] Newman, J. C., "Fracture Analysis of Surface and Through Cracked Sheets and Plates", Journal of Engineering Fracture Mechanics, Vol. 5, No. 3, 1973.

[57] Smith, F. W. and Sorensen, D. R., "The Semi-elliptical Surface Crack--A Solution by the Alternating Method", International Journal of Fracture, Vol. 12, No. 1, pp. 47-58, 1976.

[58] Hellen, T. K. and Dowling, A. R., "Three Dimensional Crack Analysis Applied to an LWR Nozzle-Cylinder Intersection", International Journal of Pressure Vessels and Piping, Vol. 3, pp. 57-73, 1975.

[59] Reynen, J., "On the Use of Finite Elements in Fracture Analysis of Pressure Vessel Components", ASME 75-PVP-20, 1975.

[60] Derby, R. W., "Shape Factors for Nozzle Corner Cracks", Experimental Mechanics, Vol. 12, No. 12, pp. 580-584, 1972.

[61] Hall, L. R. and Finger, R. W., "Fracture and Fatigue Growth of Partially Embedded Flaws", Proceedings of the Air Force Conference on Fatigue and Fracture of Aircraft Structures and Materials (AFFDL TR-70-144), pp. 235-262, 1970.

[62] Newman, J. C., "Predicting Failure of Specimens with Either Surface Cracks or Corner Cracks at Holes", NASA TN D-8244, 1976.

[63] Shah, R. C., "Stress Intensity Factors for Through and Part-Through Cracks Originating at Fastener Holes", Mechanics of Crack Growth, ASTM STP 590, 1975.

[64] Frocht, M. M., Photoelasticity, John Wiley and Sons, 1948.

[65] Jessop, H. T. and Harris, F. C., Photoelasticity, Principles and Methods, Dover, 1952.

[66] Kuske, A. and Robertson, G., Photoelastic Stress Analysis, John Wiley and Sons, 1974.

[67] Tardy, M. H. L., "Methode pratique d'examen de mesure de la birefringence des verres d'optique", Rev. d'Optique, Vol. 18, pp. 59-69, 1929.

APPENDIX

Since there are many excellent references which present the details of the photoelastic method such as [64-66] it is not the intention of the author to dwell upon the details here. However, a brief overview of photoelasticity and its application to the current problem of stress intensity determination does seem appropriate.

Many transparent materials which are ordinarily optically isotropic become optically anisotropic when they are stressed. This effect normally persists only while the loads are maintained but may be permanently induced through the stress freezing process. The phenomenon is known as double refraction and is the basis of the photoelastic method.

When a photoelastic material is stressed and a ray of light enters along one of the directions of principal stress the light is divided into two component waves, each with its plane of vibration or polarization parallel to one of the principal planes of stress. The light travels along these two paths with different speeds, which depend upon the magnitudes of the principal stresses in the material.

If the two waves are brought together in a crossed circular polariscope an interference pattern can be observed. With monochromatic light the interference pattern is a series of dark and light bands as can be seen in Figure 5.4 and are called stress fringes. The dark fringes are assigned an integral fringe order n', beginning with n' = 0, and are proportional to the maximum in-plane shear stress as noted in equation (2.6).

If white light is used as the source for the polariscope, the resulting interference pattern appears as a spectrum of colors. The border between bands of rose pink and pale green corresponds to the exact center of the dark fringes observed with monochromatic light. It is thus possible to accurately determine the center of fringes such as those pictured in Figure 5.4.

When the number of fringes is such that the photoelastic pattern does not form a satisfactory basis for obtaining a sufficient quantity of data points, it becomes necessary to measure fractional fringe orders. In this case the Tardy Method is applied. A plane polariscope is used to determine the directions of the principal planes of stress at the locations where data is desired. The model is then oriented such that the principal planes of stress are parallel to the polarizing axes of the polaroids of the crossed circular polariscope. If the second polaroid (the analyzer) is rotated clockwise an angle β degrees from its initial orientation, the fringe orders decrease by a quantity $\beta/180$ [67]. It is through the application of this procedure that many more data points appear in Figure 5.5 than the number of fringes which may be observed in Figure 5.4.

The preceding brief introduction to photoelasticity will simplify an explanation of the details of the data taking process. After obtaining a slice of material at a desired location along the flaw border, the slice is viewed in a plane polariscope. The directions of the principal planes of stress along the line corresponding to the direction of fringe spreading ($\theta = \frac{\pi}{2}$ for Mode I loading) are determined. For all slices studied it was found that the principal direction was a constant along the direction of fringe spreading on one side of the crack in the region where data were obtained.

The slice is then oriented in the proper manner in a crossed circular polariscope for the application of the Tardy Method. The data needed for the determination of the stress intensity factor reduces to the fringe order, n', and the distance from the crack tip to the fringe along the direction of fringe spreading, r. These quantitites are measured for the highest integral order fringe which corresponds to the one closest to the crack tip. The analyzer is then rotated clockwise 18 degrees so that the fringe order is reduced by 0.1. The distance from the crack tip to this fringe is then measured and the process is repeated until about two dozen sets of measurements are obtained.

From the data, the normalized apparent stress intensity factor may be calculated from equations (2.6) and (2.10) and their corresponding values of the square root of the normalized distance from the crack tip may be used to construct a graph such as Figure 5.5. Data at an $(r/a)^{\frac{1}{2}}$ less than approximately 0.2 is generally ignored due to the effects discussed in Chapter IV. A least squares analysis is used to fit a straight line through the data outside of $(r/a)^{\frac{1}{2}} \approx 0.2$, which corresponds to the region in which the data exhibit linear behavior. The straight line is then extrapolated to $(r/a)^{\frac{1}{2}} = 0$ and the normalized stress intensity factor is obtained as discussed in Chapter II.

VITA

The author was born in New York City on February 10, 1953. His initial education was a product of the New York City public school system, concluding with graduation from The Bronx High School of Science in June 1969. In September he entered Polytechnic Institute of Brooklyn and in May 1973 was awarded the degrees of Bachelor of Science (Aerospace Engineering) in Honors and Master of Science (Applied Mechanics).

The author moved to Blacksburg, Virginia during the summer of 1973 and since September 1973 has been enrolled at Virginia Polytechnic Institute and State University pursuing the degree of Doctor of Philosophy (Engineering Mechanics) while under employment at the same institution as Instructor of Engineering Science and Mechanics.

The author is an active member of several professional societies and also holds membership in Sigma Xi.

At the time of this writing the author has accepted a National Research Council Resident Research Associateship at the Air Force Materials Laboratory, Wright-Patterson Air Force Base, Dayton, Ohio beginning in December 1976.

Mitchell Jolles

A PHOTOELASTIC TECHNIQUE FOR THE DETERMINATION OF STRESS INTENSITY FACTORS

by

Mitchell Jolles

(ABSTRACT)

A technique for obtaining values of the stress intensity factor from photoelastic data for three dimensional cracked body problems is described. The stress intensity determination is accomplished without resorting to stress separation methods through employing an expression for the maximum in-plane shearing stress consisting of a singular term which is related to the stress intensity factor and a constant term which is related to the regular stress field. The technique itself identifies the zone dominated by the singular stresses.

The effects of using artificial cracks and a model material which exhibits a Poisson's ratio $\nu = 0.5$ are assessed. The application of the technique to a variety of technologically important three dimensional problems is illustrated for Mode I loading and combined Mode I - Mode II loading. The major advantages and limitations of the technique are discussed.

Replications of identical test geometries indicate a scatter of the stress intensity factor determination of less than ± 5%. It is concluded that the method is a valid means for the independent determination of values of the stress intensity factor.